

Global patterns of radiated seismic energy and apparent stress

George L. Choy

U.S. Geological Survey, Denver, Colorado

John L. Boatwright

U.S. Geological Survey, Menlo Park, California

Abstract. Radiated energies from shallow earthquakes with magnitudes ≥ 5.8 that occurred between 1986 and 1991 are used to examine global patterns of energy release and apparent stress. In contrast to traditional methods which have relied upon empirical formulas, these energies are computed through direct spectral analysis of broadband seismic waveforms. Velocity-squared spectra of body waves are integrated after they have been corrected for effects arising from depth phases, frequency-dependent attenuation, and focal mechanism. The least squares regression fit of energy E_S to surface wave magnitude M_S for a global set of 397 earthquakes yields $\log E_S = 4.4 + 1.5M_S$, which implies that the Gutenberg-Richter relationship overestimates the energies of earthquakes. The least squares fit between E_S and seismic moment M_0 is given by the relationship $E_S = 1.6 \times 10^{-5}M_0$, which yields 0.47 MPa as the average global value of apparent stress. However, the regression lines of both E_S - M_S and E_S - M_0 yield poor empirical predictors for the actual energy radiated by any given earthquake; the scatter of data is more than an order of magnitude about each of the regression lines. On the other hand, global variations between E_S and M_0 , while large, are not random. When subsets of E_S - M_0 are plotted as a function of seismic region and faulting type, the scatter in data is substantially reduced. The E_S - M_0 fits for many seismic regions and tectonic environments are very distinctive, and a characteristic apparent stress τ_c can be derived. The lowest apparent stresses (< 1.5 MPa) are associated with thrust earthquakes at subduction zones. The highest apparent stresses (> 3.0 MPa) are associated with strike-slip earthquakes that occur at oceanic ridge-ridge transforms and in intraplate environments seaward of island arcs. Intermediate values of apparent stress ($1.5 < \tau_a < 3.0$ MPa) are associated with strike-slip earthquakes at incipient or transitional plate boundaries. In general, the dominant mode of failure for a tectonic environment is associated with the faulting type that has the lowest apparent stress. An energy magnitude M_E can complement moment magnitude M_W in describing the size of an earthquake. M_E , being derived from velocity power spectra, is a measure of seismic potential for damage. M_W , being derived from the low-frequency asymptote of displacement spectra, is more physically related to the final static displacement of an earthquake. When earthquake size is ranked by moment, a list of the largest events is dominated by earthquakes with thrust mechanisms. When earthquake size is ranked by energy, the list of the largest events is dominated by strike-slip earthquakes.

Introduction

The seismic energy radiated by earthquakes is a fundamental measure of earthquake size. In theory, its computation simply requires an integration of radiated energy flux in velocity-squared seismograms. In practice, energy has historically almost always been estimated with empirical formulas. The empirical approach was favored for two major reasons. First, until this past decade the dominant form of seismic data has been analog, a format which is not amenable to spectral processing on a routine basis. Moreover, an accurate estimate of radiated energy requires the analysis of spectral information both above and below the corner frequency of an earthquake, where energy density is most strongly peaked. Before the de-

velopment of broadband forced-balance seismometers, the response of most conventional seismographs (such as that of the Worldwide Standardized Seismograph Network) was shaped inversely to the spectrum of Earth noise in order to optimize signal detection. However, the stratagem of filtering out peaks in the spectrum of Earth noise also effectively filtered out information between approximately 0.1–1.0 Hz within which is found the corner frequency of most large earthquakes. The difficulties in processing analog data were thus compounded by the limitations in retrieving reliable spectral information over a broad bandwidth. Fortunately, theoretical and technological improvements in the past decade have combined to remove the practical impediments to the direct computation of radiated energy. *Boatwright and Choy* [1986] have shown that (1) data with the requisite broad bandwidth are now recorded digitally and (2) frequency-dependent corrections for source mechanism and wave propagation are better understood now than at the time empirical formulas were developed. The first condi-

This paper is not subject to U.S. copyright. Published in 1995 by the American Geophysical Union.

Paper number 95JB01969.

tion was met by the worldwide deployment of digitally recording seismograph networks and arrays with broadband capability, beginning with the installations of the Graefenberg array in Germany in 1975 and of the Global Digital Seismograph Network (GDSN) operated by the U.S. Geological Survey in 1976. Sources of broadband digital data are now complemented by many other global and regional networks such as the Global Seismographic Network (GSN), Chinese Digital Seismograph Network (CDSN), GEOSCOPE, and TERRASCOPE. Although raw data are often not directly proportional to either displacement or velocity over a wide and continuous range of frequencies, broadband displacement and velocity records are easily obtained using the methods such as described by *Harvey and Choy* [1982], which uses multichannel instrument deconvolution whenever necessary to recombine data recorded on separate but overlapping frequency bands. The second condition is satisfied by the spectral method described by *Boatwright and Choy* [1986], which accommodates effects on waveforms arising from the interference of surface-reflected arrivals, from the frequency dependence of attenuation, from the partition of energy between compressional and shear waves, and from the double-couple radiation pattern of earthquake faulting. Since November 1986, the National Earthquake Information Center (NEIC) has been using the algorithm of *Boatwright and Choy* [1986] to compute radiated energies for shallow earthquakes of $m_b > 5.8$ on a routine basis.

We have compiled the energies of 397 shallow earthquakes with $m_b > 5.8$. Of these 368 are taken from listings of the NEIC for earthquakes occurring between November 1986 and December 1991. The database is complemented by another 28 energies taken from studies of earthquakes that occurred before 1986. In this paper, we first compare direct estimates of the radiated energies (E_S) of the global data set with other estimates of earthquake size, namely, magnitude (M_S) and moment (M_0). These comparisons of global data immediately show that no single relationship can adequately describe the large scatter in parameter space covered by energy as a function of either magnitude or moment. Fortunately, the database is now sufficiently large that we are able to examine the characteristics of energy radiated by subsets of earthquakes. The primary objective of this paper is to conduct the first systematic search for variations in directly computed estimates of radiated energy as a function of focal mechanism, seismic region, and tectonic environment. Time-dependent parameters, such as repeat time, that would require decades or centuries for confirmation are outside the scope of this paper. Another objective of this paper is to present a global map of seismic energy release. As apparent stress is defined as the ratio of E_S/M_0 [e.g., *Wyss and Brune*, 1968; *Snoke et al.*, 1983; *Choy and Boatwright*, 1981], our investigation of systematic variations in E_S/M_0 simultaneously yields a global mapping of apparent stress. Finally, we show that energy, as an independently computed source parameter, can complement moment and magnitude in assessing the potential for earthquake damage and tsunami generation.

Method

In this section we describe briefly the method used by *Boatwright and Choy* [1986] to make teleseismic estimates of energy from direct measurement of seismograms. This method consists of two key elements. The first element is an algorithm for energy which incorporates corrections to body waves for effects

that arise from the rupture process and for effects that are incurred during propagation in Earth. For shallow earthquakes where the source functions of direct and surface-reflected body wave arrivals may overlap in time, the expression relating radiated energy to the energy flux of a P wave group (consisting of P , pP , and sP) is given by

$$E_S = 4\pi \langle F^P \rangle^2 (R^P/F^{gP})^2 \varepsilon_{gP}^* \quad (1)$$

where ε_{gP}^* is the integral of the square of the ground velocity, taken over the duration of the body wave arrival,

$$\varepsilon_{gP}^* = \int_0^\infty \dot{U}(t)^2 dt \quad (2)$$

Here \dot{U} is velocity, which must be corrected for frequency-dependent attenuation; $\langle F^P \rangle^2$ is the mean-square radiation-pattern coefficient for P waves; R^P is the P wave geometrical spreading factor; F^{gP} is the generalized radiation pattern coefficient for the P wave group defined as

$$(F^{gP})^2 = (F^P)^2 + (F^{pP})^2 + \frac{2\alpha q}{3\beta} (F^{sP})^2 \quad (3)$$

where F^i are the radiation-pattern coefficients for $i = P$, pP , and sP and q is 15.6, the ratio of S wave energy to P wave energy from *Boatwright and Choy* [1986]. The correction factors explicitly take into account our knowledge that the earthquake is a double couple, that measurements of the waveforms are affected by interference from depth phases, and that energy is partitioned between P and S waves. Another advantage that accrues to using generalized radiation pattern coefficient is that the effects of nodal takeoff angles are smoothed out. For pure vertical strike-slip earthquakes, the average radiation pattern coefficient for n stations,

$$\bar{F}^{gP} = \frac{1}{n} \left(\sum (F^{gP})^2 \right)^{1/2},$$

is about 0.25. For pure dip-slip earthquakes, \bar{F}^{gP} is about 1.00. Moreover, for an ensemble of stations, \bar{F}^{gP} remains relatively stable for small changes in focal mechanism. This is particularly important for strike-slip earthquakes where the amplitudes of P , pP , and sP can each change rapidly with small changes in nodal plane. The largest variation in \bar{F}^{gP} is about 25% for changes in strike, dip, and rake of $\pm 10^\circ$. In routine use, we make no corrections for possible directivity. In an extension of the method, *Boatwright and Choy* [1989] found that the increase in energy estimates when incorporating an explicit correction for directivity was relatively small, the largest being 20–40%.

The bandwidth of the attenuation correction we apply should be commensurate with the bandwidth of the data we analyze. As the data are broadband, typically from 0.01 Hz to about 5.0 Hz, the attenuation correction must be frequency-dependent [*Cormier*, 1982]. The correction is easier to realize in the frequency domain. Parseval's theorem is used to transform (2),

$$\varepsilon_{gP}^* = \frac{1}{\pi} \int_0^\infty |\dot{u}(\omega)|^2 \exp(\omega t_\alpha^*) d\omega, \quad (4)$$

where t_α^* is proportional to the integral over ray path of the imaginary part of complex slowness in an anelastic Earth. An

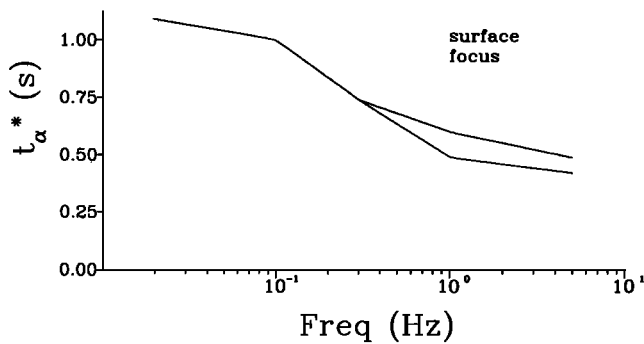


Figure 1. Teleseismic t_{α}^* derived by *Choy and Cormier* [1986] plotted as a function of frequency for a surface focus source and a surface receiver at a distance of 60° . The split in the curve at frequencies higher than 0.3 Hz indicates the variation in regional t_{α}^* expected for different receiver sites. In practice, we use the mean of the two curves for the expected attenuation.

appropriate operator, valid over the requisite broad bandwidth, is described by *Choy and Cormier* [1986] and shown in Figure 1. The t_{α}^* of the P wave operator ranges from 1.0 s at 0.1 Hz to 0.5 s at 2.0 Hz. Where signal falls below the noise level (typically at 2.0–3.0 Hz), the velocity spectrum is approximated by a curve that falls off by ω^{-1} .

Teleseismic SH and SV wave groups from shallow earth-

quakes can be analyzed through a straightforward extension of (1) as described by *Boatwright and Choy* [1986]. However, the SH and SV wave groups suffer substantially more attenuation in propagation through the Earth than the P wave group. The loss of seismic signal due to attenuation typically precludes using spectral information for frequencies higher than about 0.2–0.3 Hz for all but the largest earthquakes. For the routine estimation of energy, it is easier and more accurate to use the P wave group. The SH wave group for a few of the very large earthquakes ($E_s > 5.0 \times 10^{16}$ N m), which release a substantial amount of energy below 0.2–0.3 Hz, can be used to confirm the self-consistency of the attenuation model and the energy estimate from P waves. The energies estimated from SH waves are usually in agreement with the P wave energies by better than 30%. For instance, for the Gulf of Alaska earthquake of March 6, 1988 (M_w 7.8; M_s 7.6), which had a predominantly strike-slip focal mechanism, the P and SH estimates of energy were 9.7×10^{16} N m and 9.5×10^{16} N m, respectively.

The second element essential to the approach is that the algorithm must be applied to data that are commensurate with the dynamics of the source. In contrast to magnitude, which averages amplitudes measured from only a single frequency, the estimate of energy requires an integration over the suite of frequencies where the energy density is most strongly peaked. Band-limited seismograms will suffice for computing magnitude, but data for computing energy must contain information about the corner frequency of an earthquake, a quantity that

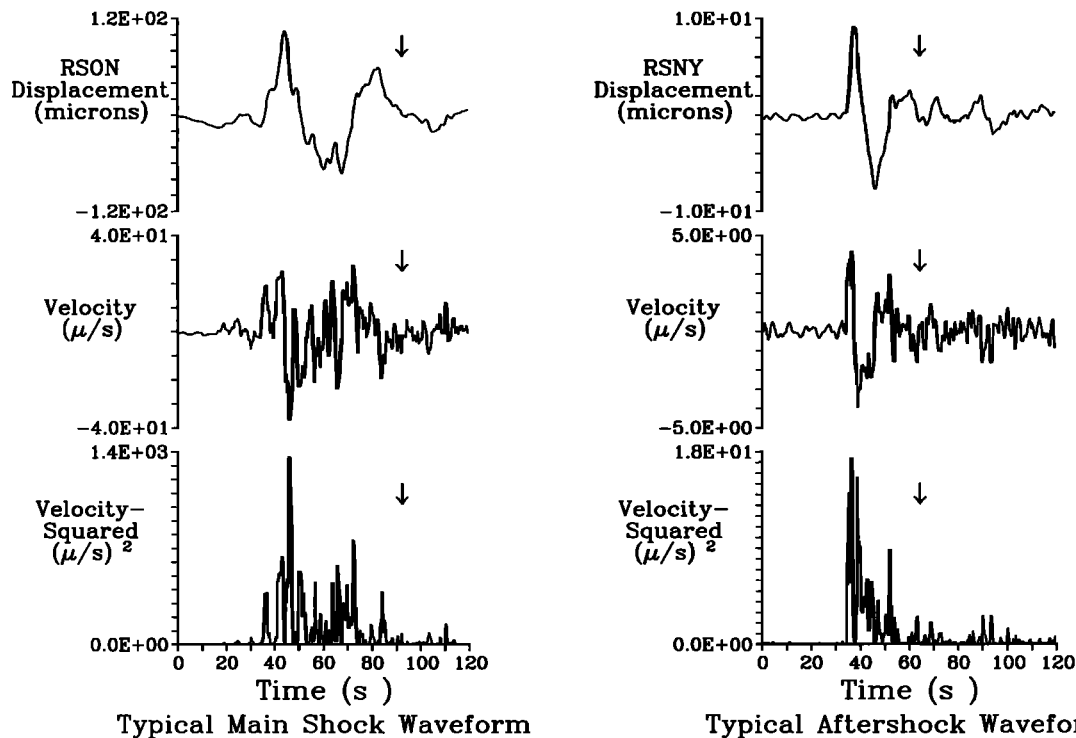


Figure 2. (left) Broadband displacement, velocity, and velocity-squared records for the large (M_s 7.8) Chilean earthquake of March 3, 1985. Rupture complexity, in the form of a tiny precursor and a number of subevents, is typical for large earthquakes. (right) Broadband displacement, velocity, and velocity-squared records for an aftershock (m_b 5.9) to the Chilean earthquake that occurred March 17. The waveforms are less complex than the main shock. Despite the differences in rupture complexity, duration, and amplitude, the time window over which energy arrives is unequivocal. In each part of the figure the arrows indicate when the velocity-squared amplitude has decreased to the level of the coda noise.

Table 1. Various Estimates of Moment for the March 3, 1985, Earthquake

Method	Moment, 10^{20} N m
Broadband body wave <i>Choy and Dewey</i> [1986]	3.5
Long-period body wave <i>Christensen and Ruff</i> [1986]	7.0
Centroid moment tensor Harvard	10.0
256-s surface waves <i>Monfret and Romanowicz</i> [1986]	12.0
Static dislocation <i>Barrientos</i> [1988]	16.0

may vary considerably from earthquake to earthquake depending on source size and rupture complexity. The data most suited for this task are broadband waveforms which, for teleseismically recorded earthquakes (m_b greater than about 5.5), we define as having a flat spectral response to ground displacement or velocity between 0.01 Hz and 5.0 Hz. This bandwidth is considered broadband because (1) it incorporates the corner frequency of an earthquake; (2) it includes enough high frequencies to compute an energy; and (3) for all except the greatest earthquakes, it includes enough low frequencies to compute a moment. An advantage that accrues to using broadband data is that the computation of energy becomes robust in that the rupture process need only be sampled over the time interval in which the fault is dynamically rupturing. As shown by the example in Figure 2, the criteria for delimiting the time window are generally unequivocal regardless of the complexity of rupture or the size of the earthquake. The arrival of energy is obviously identified with the onset of the direct P wave. The radiation of energy effectively ceases when the amplitude of the velocity-squared signal merges with the coda noise. In contrast, *Choy and Dewey* [1986] point out that if a significant component of the rupture process is quasi-static or aseismic, measurements of scalar moment can become frequency-

dependent. As an example, Table 1 compares the moments derived from a variety of methods for the Valparaiso earthquake of March 3, 1985 (M_s 7.8). These moment estimates vary by over a factor of 4, increasing as the dominant frequency in the method of computation decreases. Indeed, frequency dependence in moment, exceeding a factor of 4 in the frequency range 1.0–10.0 mHz, has been found for a number of large earthquakes [e.g., *Silver and Jordan*, 1983]. The fact that source properties derived from a low-frequency inversion may describe physically different aspects of the rupture process than source properties derived from broadband data is another compelling reason for computing radiated energy directly rather than by an empirical relationship with magnitude or moment.

The computation of radiated energy using (3) also requires a correction for focal mechanism. The Monthly Listings of the Preliminary Determination of Epicenters (PDE) publishes focal mechanism solutions derived from three different methods: (1) the radiation pattern of P wave first motions (FM); (2) the inversion using a body wave moment tensor (BMT) [*Sipkin*, 1982]; and (3) the inversion using a centroid moment tensor (CMT) [*Dziewonski et al.*, 1981]. Although the solutions from the three methods are rarely in full agreement, the energy computation varies by less than a factor of 2 for moderate variations in the principal axes of predominantly dip-slip mechanisms. This is the case for about 70% of the events. However, the differences in the solutions for about 15% of the earthquakes in our data set are drastic enough (two examples are shown in Figure 3) that the correct choice of mechanism is critical to the energy computation. Although some of the differences in the mechanisms may be attributed to intrinsic differences in the algorithms [*Sipkin*, 1982], the description of the rupture process may also differ depending on the spectral bandwidth emphasized by each method. The P wave first-motion solution, for instance, is most sensitive to the onset of initiation nucleation. In contrast, moment tensor inversions, by utilizing low-frequency data, tend to average out the details of the rupture process over tens of seconds. Ideally, radiated

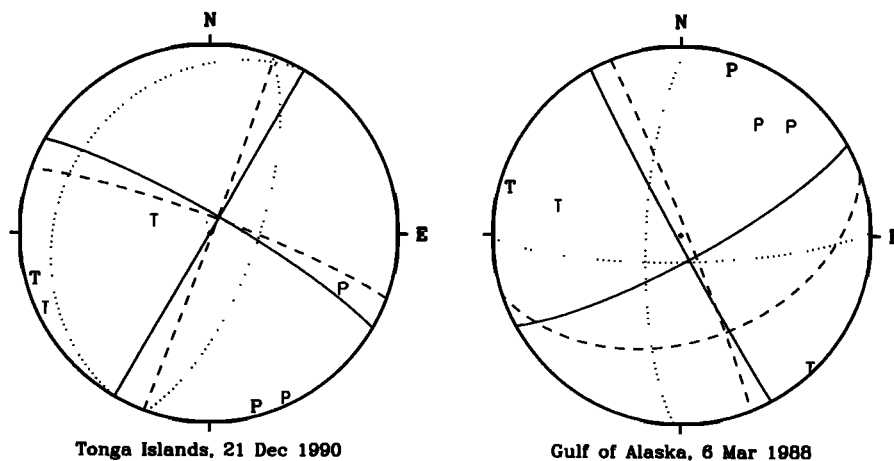


Figure 3. For about 15% of the earthquakes studied significant differences exist among the different double-couple focal mechanisms published in the Monthly Listings of the Preliminary Determination of Epicenters. Typical differences for two such events are shown. The three mechanisms in each focal sphere are a P wave first-motion solution (solid line), a U.S. Geological Survey body wave moment tensor (dashed line), and a Harvard centroid moment tensor (dotted line). For the correct computation of E_s , we must either choose or derive a mechanism that is compatible with broadband waveforms.

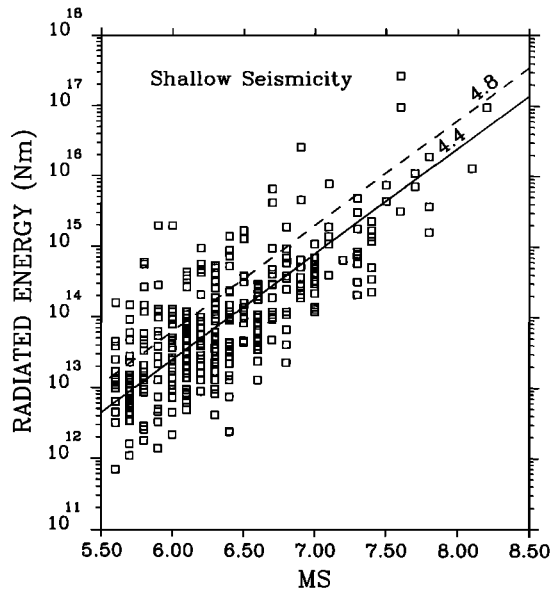


Figure 4. Radiated energy (E_S) of the global data set plotted as a function of surface wave magnitude (M_S). The energy predicted by the Gutenberg-Richter formula, $\log E_S = 4.8 + 1.5M_S$ (in units of Newton meters), is shown by the dashed line. From a least squares regression, the best fitting line with the slope of 1.5 is $\log E_S = 4.4 + 1.5M_S$. For most earthquakes the Gutenberg-Richter formula overestimates the actual energy. It is also evident that no simple formula can predict energy from magnitude. For any given M_S the actual energy can vary by 2 orders of magnitude.

energy should be computed from the focal mechanism that is most compatible with the dynamic part of the rupture process. For the events that occurred before 1986, we use focal mechanism solutions taken from special studies in which the solutions were derived explicitly from the modeling of broadband waveforms. For the majority of events, which occurred after 1987, the most energy-compatible mechanism is selected from among the three double-couple fault plane solutions published in the Monthly Listings. The most energy-compatible mechanism is that solution which predicts broadband synthetics that are most consistent with the polarities and amplitudes of the observed broadband waveforms. We note that between 1987 and 1988, the National Earthquake Information Center (NEIC) found the P wave first-motion solution to be the overwhelming choice for earthquakes with substantial strike-slip components. However, it was usually not invoked for predominantly dip-slip earthquakes because the distribution of teleseismic P waves about the focal sphere was generally insufficient to constrain both nodal planes. The resolution of the first-motion solution was improved starting in May 1988 as the NEIC began to complement the P wave data with polarities of pP and sP , whenever they were distinguishable in the broadband waveforms. With the increased constraint on nodal planes, the frequency with which the first-motion solution was chosen as the energy-compatible mechanism increased from about one-third to two-thirds of the events studied. This is consistent with our observation that the quasi-static processes inferred from low-frequency inversion may not be accurate representations for the processes during dynamic rupture. Table 5, which lists the events in our global data set, includes the focal mechanism that we found to be most energy-compatible.

In subsequent sections of this paper we compare estimates of radiated energy with seismic moment. To discern patterns of energy and moment release, we need moments computed by a uniform method. Unless otherwise noted, we use for scalar moments the CMT value found in the Monthly Listings. The BMT value is also published, but the centroid moment is more expedient because it was computed for 98 more events over the time period covered by our data set. On average, our conclusions are qualitatively unchanged regardless of whether the CMT or BMT moments are used. The moments are usually in agreement for earthquakes smaller than 10^{20} N m [Sipkin, 1986]. We also note that Houston [1990] computed energies for seven large earthquakes using a method that applied a water level correction to generalized radiation pattern coefficients and a constant $t_\alpha^* = 0.7$ s for attenuation. Houston's energies were in agreement with ours by at least a factor of 2.

Measures of Earthquake Size From Global Seismicity

When it is directly computed, energy can be compared to other estimates of earthquake size such as magnitude and moment rather than being dependent on them. In Figure 4 the radiated energies for our set of global shallow earthquakes are plotted against their magnitudes, M_S . In the Gutenberg-Richter formula, energy is related to magnitude through

$$\log E_S = a + bM_S, \quad (5)$$

where the a and b values are 4.8 and 1.5, respectively. This relationship is plotted as a dashed line in Figure 4. The least squares regression fit between the actual energies and magnitude, assuming a b value of 1.5, yields

$$\log E_S = 4.4 + 1.5M_S \quad (6)$$

which is plotted as the solid line in Figure 4. The new a value, based on 378 earthquakes with an associated M_S , indicates that on average the original Gutenberg-Richter formula overestimated the radiated energy by a factor of 2. Regardless of which set of constants is a better fit to the data, however, the utility of a formula that predicates energy on a value of magnitude is moot. For any given value of M_S , the distribution of energy estimates spans almost 2 orders of magnitude about the mean value. No single formula can meaningfully describe such a large parameter space. Other methods of computing energy also conclude that the Gutenberg-Richter formula overestimates energy (e.g., Houston [1990] from six global earthquakes and Kikuchi and Fukao [1988] from long-period seismograms).

When radiated energy for global shallow earthquakes is plotted against seismic moment (Figure 5a), the best fit by least squares regression of E_S on M_0 (solid line) yields

$$E_S = 1.6 \times 10^{-5} M_0. \quad (7)$$

Since apparent stress for a particular earthquake, τ_a , can be obtained from energy and moment by using

$$\tau_a = \mu E_S / M_0, \quad (8)$$

where μ is the average rigidity, the regression line can be expressed in terms of an average apparent stress $\bar{\tau}_a$. For global seismicity, $\bar{\tau}_a$ is 0.47 MPa. Since the E_S - M_0 data are lognormally distributed, we quantify scatter by calculating the standard deviation of the logarithms of the apparent stresses. The antilog of this standard deviation is called the geometric

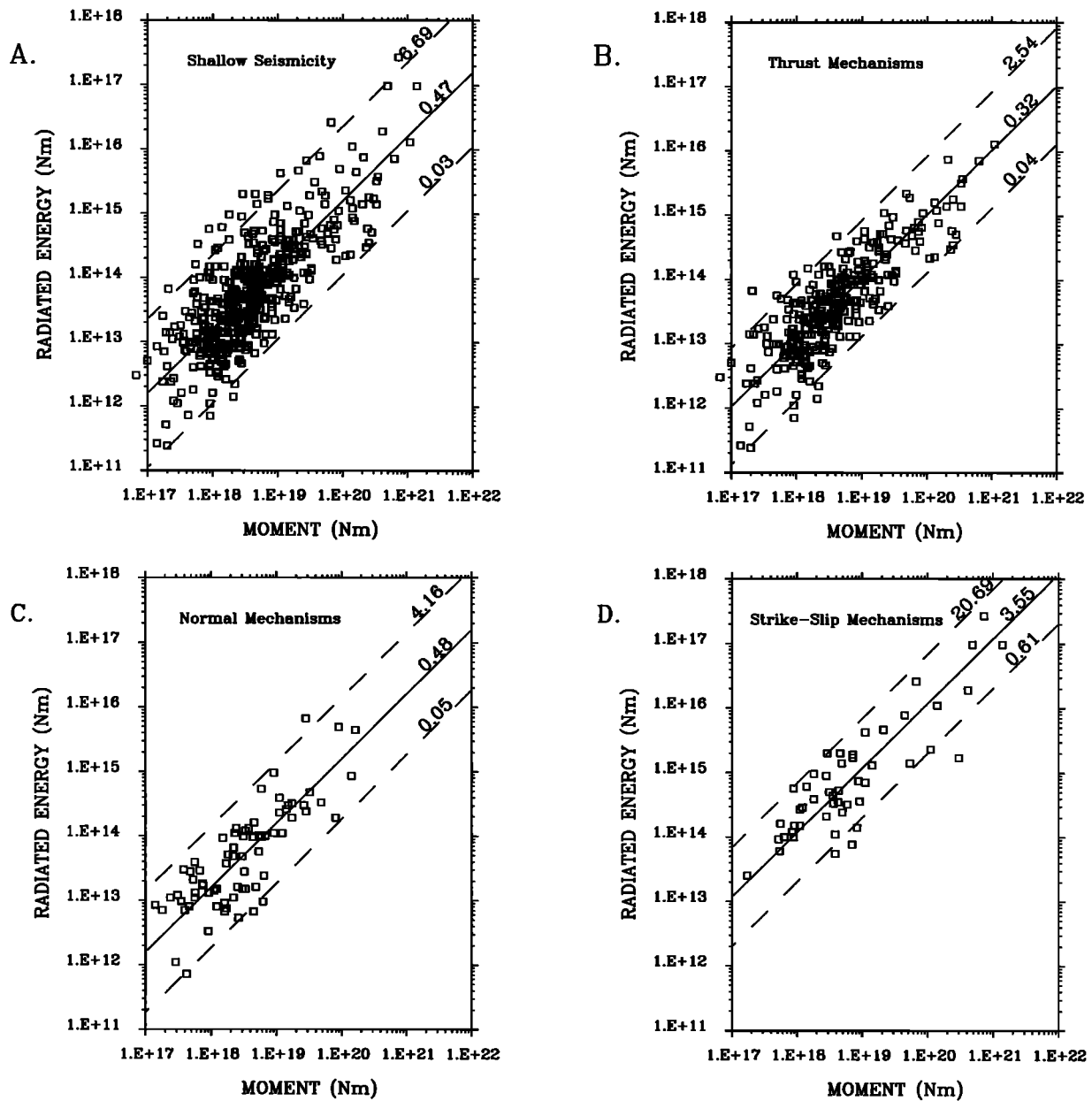


Figure 5. (a) Radiated energy of 394 shallow focus earthquakes plotted as a function of seismic moment. The slope, E_S-M_0 , of the least squares linear regression (solid line) yields a global average apparent stress ($\bar{\tau}_a$) of 0.47 MPa. The 95% geometric spread (or width of distribution) about the regression line is indicated by the dashed lines. It is evident that no simple relation exists between E_S and M_0 . (b) The E_S-M_0 plot for 270 thrust-fault earthquakes. The linear regression yields a geometrically averaged apparent stress of $\bar{\tau}_a$ 0.31 MPa. The 95% geometric spread (dashed lines) is substantially smaller for the subset of thrust-fault earthquakes than for the composite of global earthquakes. (c) The E_S-M_0 plot of 69 normal-faulting earthquakes. The $\bar{\tau}_a$ of 0.48 MPa is higher than the $\bar{\tau}_a$ for thrust-fault earthquakes. However, the 95% geometric spread (dashed lines) is wider than that for the population of thrust-fault earthquakes. (d) The E_S-M_0 plot of 55 strike-slip earthquakes. The apparent stress for strike-slip earthquakes appears to be fundamentally different from that of dip-slip earthquakes. Although the geometric spread is somewhat large, the $\bar{\tau}_a$ for strike-slip earthquakes is 3.62 MPa, which is almost an order of magnitude higher than the $\bar{\tau}_a$ for the dip-slip earthquake populations.

spread; this parameter represents a multiplicative factor that indicates the width of the (asymmetric) distribution of the apparent stress. The geometric spread corresponding to two standard deviations (95% of the width of the data) is indicated by dashed lines. For global seismicity the spread about a mean of 0.47 MPa ranges between 0.03 and 6.69 MPa. Thus the scatter about the regression lines of E_S-M_0 is comparable to the scatter in

the E_S-M_S plot. Clearly, accumulating more data for the purpose of refining the coefficients in the empirical formulas would be a moot endeavor. Improving the accuracy of the a and b values will not yield any further physical insight into earthquake characteristics. We investigate instead the causes of the scatter in the relationship between energy and moment.

The global earthquake population can be readily decom-

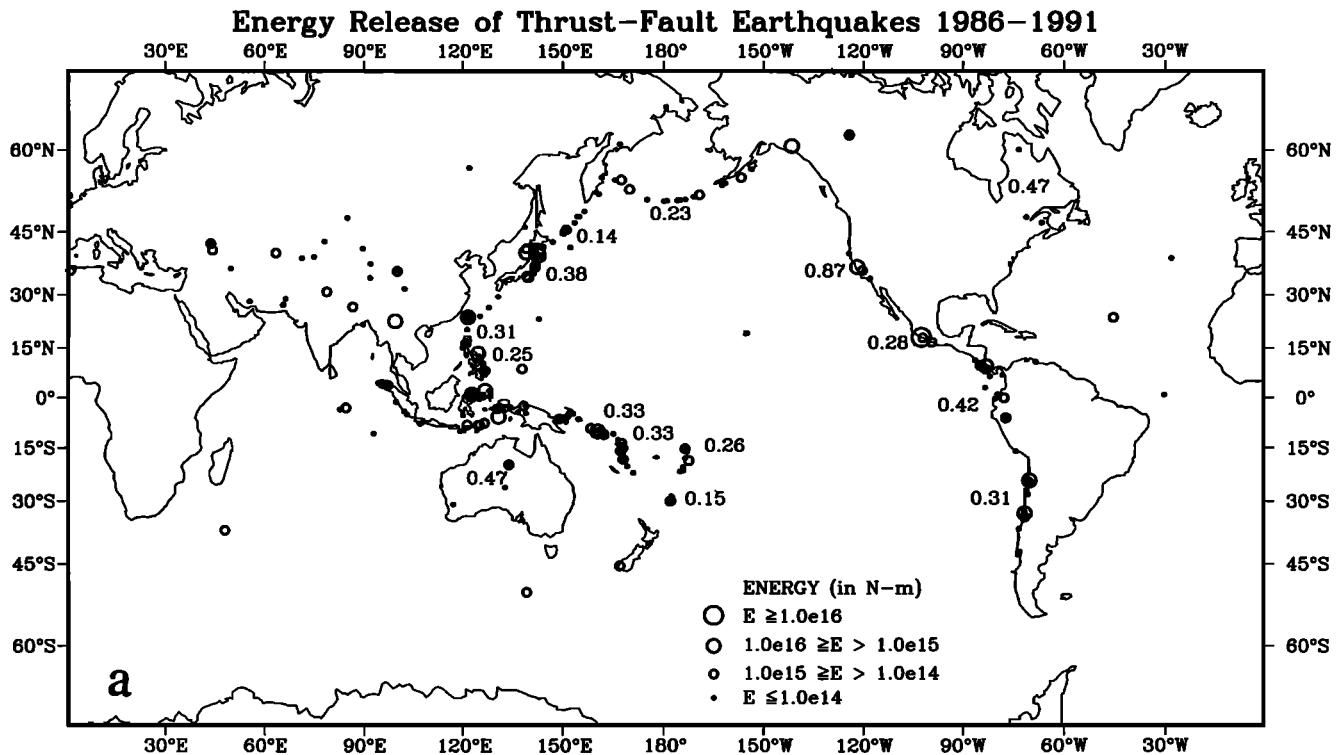


Figure 6. Global patterns of energy release for all large ($E_S > 10^{10}$ N m) shallow earthquakes between November 1986 and December 1991. (a) Earthquakes with predominantly thrust-fault mechanisms. The τ_a (in megapascals) is indicated for those seismic regions where the absolute spread about E_S - M_0 line is less than 1.5 MPa. (b) Earthquakes with predominantly normal-fault mechanisms. (c) Earthquakes with predominantly strike-slip faulting mechanisms.

posed into subsets based on focal-mechanism type. In Figures 5b–5d we plot E_S - M_0 for subsets of earthquakes with focal mechanisms that were either predominantly thrust, normal, or strike-slip. For each subset the regression line and its geometric spread are expressed in terms of apparent stress. Two features that are not evident in the global composite now become very prominent. First, the wide geometric spread in the E_S - M_0 relation of the global data set is largely the result of the population of normal-fault and strike-slip earthquakes. The geometric spread of thrust-fault earthquakes (which has an upper bound of 2.4 MPa) is substantially reduced relative to the global population (which has an upper bound of 9.4 MPa). A reduction, however, is not as dramatic for the normal- and strike-slip populations. A second feature is that the average apparent stress $\bar{\tau}_a$ of strike-slip earthquakes appears to be very different from that of dip-slip earthquakes. The $\bar{\tau}_a$ for strike-slip earthquakes is 3.62 MPa. This is an order of magnitude higher than the $\bar{\tau}_a$ found for dip-slip earthquakes, which are 0.31 and 0.48 MPa for thrust and normal faults, respectively. Because of the significant overlap in the geometric spreads of the three subsets, it is not unequivocal whether there are fundamental differences in $\bar{\tau}_a$ for different types of faulting. In the remainder of this paper, we examine the patterns of apparent stress that result when we further decompose our data into subsets based on tectonic setting and seismic region as well as focal mechanism. We find that the width of the geometric spread about the $\bar{\tau}_a$ is often very narrow for many subsets of data defined by a faulting type and by a tectonic setting or seismic region. The average apparent stress ($\bar{\tau}_a$) for a group of

earthquakes is called a characteristic apparent stress, τ_c , if (1) the group of data has at least five earthquakes; and (2) the absolute width of the geometric spread (the difference between the upper and lower bounds of the geometric spread) is less than about 1.5 MPa. Note that the absolute width in our definition, while sufficiently narrow to define a characteristic apparent stress, remains sufficiently wide to admit identification of differences among individual earthquakes. For instance, in the main shock-aftershock sequence associated with the Chilean earthquake of May 1985, for instance, Choy and Dewey [1986] found that the apparent stress of the main shock (0.72 MPa) was significantly higher than the apparent stresses of all but the last and largest of the major aftershocks (ranging from 0.24 to 0.51 MPa). Note that although a large apparent stress certainly implies a commensurately large stress drop, we deliberately eschew direct computation of a stress drop. While apparent stress is clearly defined through the E_S/M_0 ratio, determination of stress drop is model-dependent. Apparent stress is robust in that it does not depend on the assumed rupture geometry or model. The apparent stresses we obtain may be useful as an independent constraint on stress drops predicted by geometry-dependent models.

Thrust-Fault Earthquakes

In this section we use E_S - M_0 plots to investigate the characteristics of apparent stress for shallow earthquakes with predominantly thrust focal mechanisms. The distribution of global energy release between 1986 and 1991 for this class of earthquakes is shown in Figure 6. Almost all the thrust-fault earth-

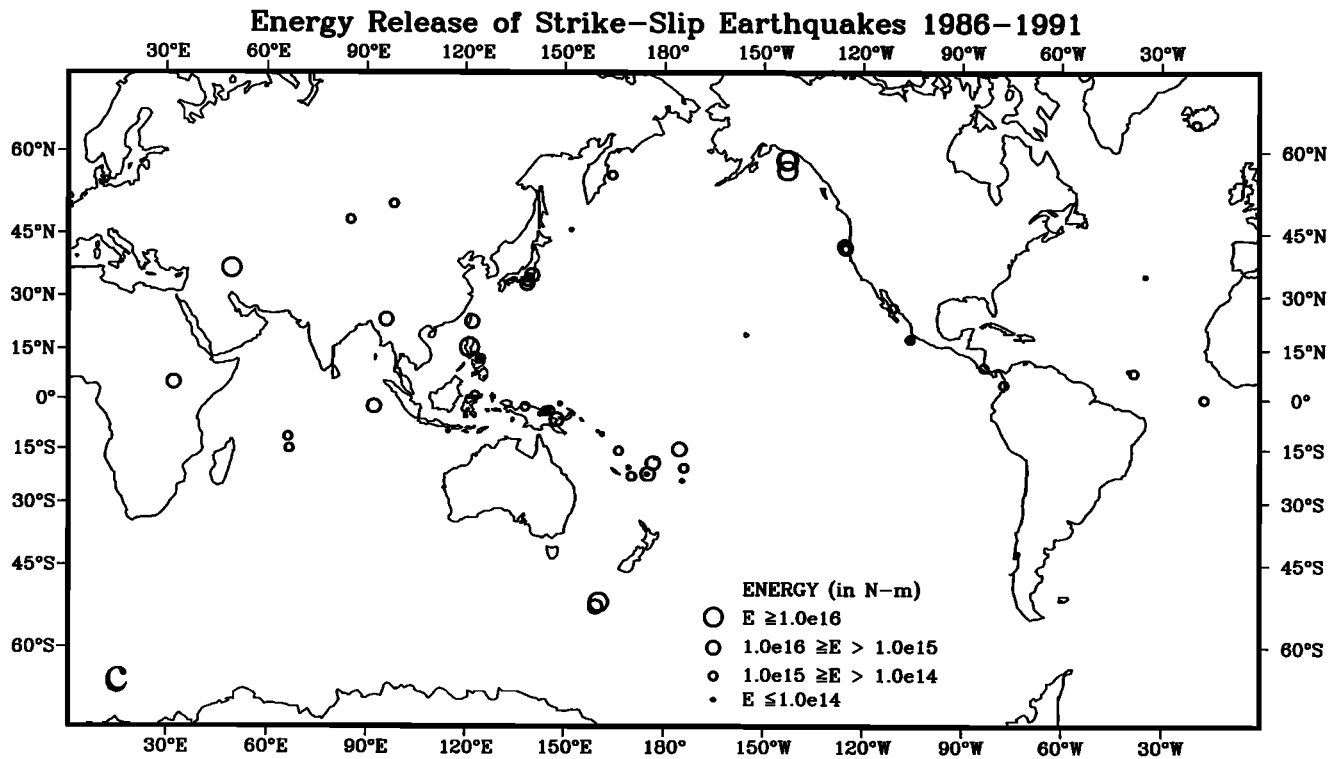
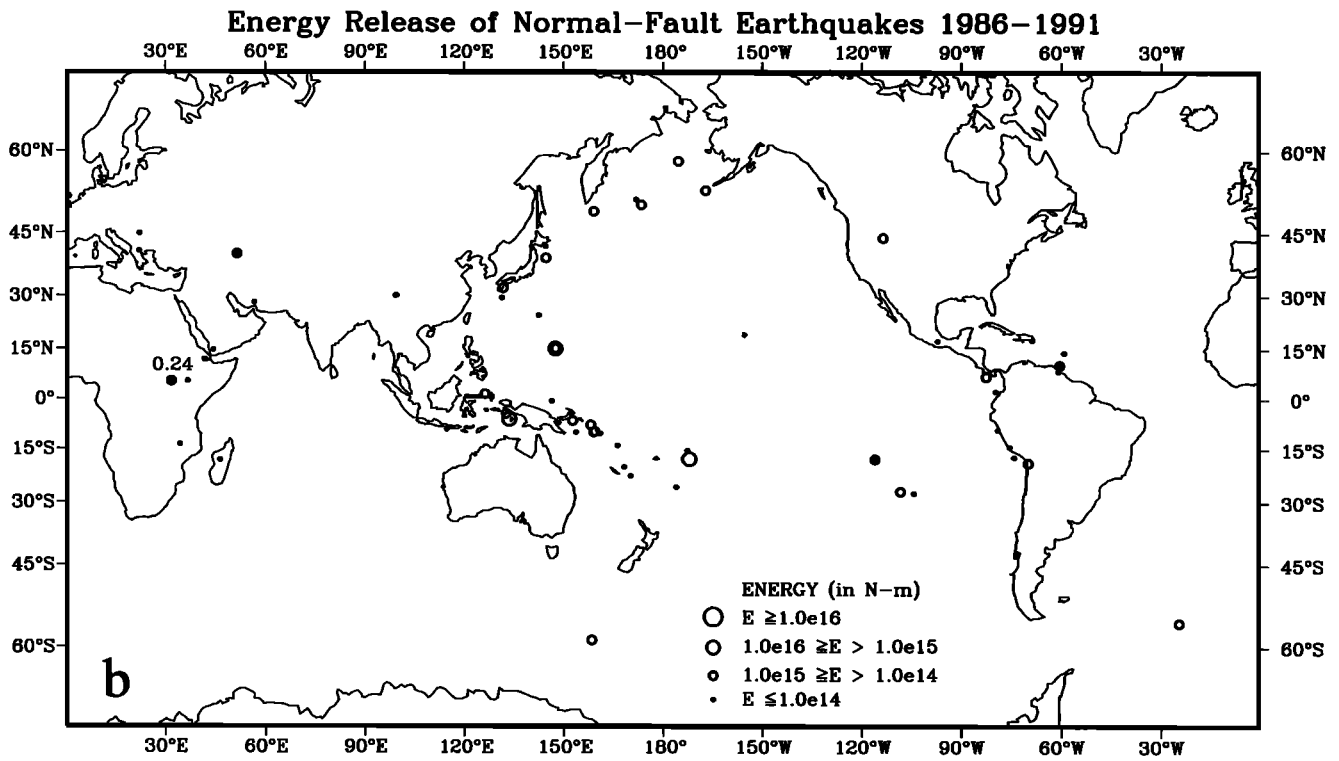


Figure 6. (continued)

quakes are concentrated in four tectonic environments which can be classified as oceanic subduction, continental collision, continental intraplate, and near-plate margin. For oceanic subduction zones, the number of earthquakes is sufficiently abundant that we can examine the relation between E_S and M_0 as

a function of particular seismic regions. Our convention for seismic region follows with slight modification the nomenclature and regionalization scheme of *Flinn et al.* [1974]. In contrast to the seismicity at oceanic subduction zones, activity at the other tectonic environments is too sparse to permit analysis

of specific seismic regions. Therefore the data sets for the other tectonic environments are a global composite of the earthquakes that occurred in similar environments. Table 2a summarizes the apparent stresses found for various tectonic environments and seismic regions.

Oceanic subduction zones. The $\bar{\tau}_a$ of thrust-fault earthquakes for all oceanic subduction zones is 0.29 MPa. However, the width of the geometric spread is still somewhat large at about 2.3 MPa. Fortunately, thrust earthquakes at subduction zones are the most dominant component of our data set, consisting of 222 earthquakes (including 15 events predating November 1986 taken from *Choy and Dewey* [1986] and *Boatwright and Choy* [1989]). For most of the active seismic regions about the circum-Pacific there are sufficient data in the E_S - M_0 plots to derive a meaningful $\bar{\tau}_a$. Most subduction zone regions have a characteristic apparent stress (τ_c), that is, an average apparent stress with an absolute spread (or width of distribution) <1.5 MPa. (In contrast, the absolute spread for the composite of all shallow thrust earthquakes is about 6.6 MPa.) These regions are listed in Table 2b as well as summarized in Figure 6. The E_S - M_0 plots for two regions which exhibit a narrow spread, the Alaska-Aleutian arc and the central Chilean subduction zone, are shown in Figure 7. Other regions with τ_c are the subduction zones bordering Middle America, Peru-Ecuador, the Kurils, Honshu, the Philippines, the Solomons, Vanuatu, Tonga-Samoa, Kermadec, and Taiwan. Most τ_c range from 0.12 to 0.33 MPa, although it is as high as 0.38 MPa

Table 2a. Average Apparent Stress $\bar{\tau}_a$ for Earthquakes as a Function of Focal Mechanism and Tectonic Setting

	$\bar{\tau}_a$, MPa	Width, $\times 10$	Number of Events
Global composites			
All shallow earthquakes	0.47	1.43	394
Thrust-fault earthquakes	0.31	0.80	270
Normal-fault earthquakes	0.48	0.87	69
Strike-slip earthquakes	3.62	0.57	55
Oceanic subduction zone			
Thrust earthquakes	0.29	0.83	222
Normal earthquakes	0.59 ^a	0.95	45
Oceanic rift zone			
Thrust earthquakes	0.62	0.31	5
Normal earthquakes	0.25	0.42	17
Strike-slip earthquakes	4.48	0.38	13
Oceanic intraplate			
Strike-slip earthquakes	6.95	0.30	16
Transitional interplate boundary			
Strike-slip earthquakes	1.50	0.17	7
Continental intraplate			
Thrust earthquakes	0.46 ^a	0.33	11
Normal earthquakes	0.95 ^a	0.14	5
Continental collision			
Thrust earthquakes	0.43	0.60	17
Normal earthquakes	0.46	0.45	5
Continental rift			
Normal earthquakes	0.25 ^a	0.43	10

As the data are lognormally distributed, the 95% width of distribution about each $\bar{\tau}_a$ is expressed in terms of a geometric spread, i.e., the logarithmic uncertainty is obtained by multiplication and division with the width as a factor. The number of events used in each group is given.

^aAlso a characteristic apparent stress τ_c for that tectonic environment. A τ_c is an average apparent stress which has an absolute spread (the difference between upper and lower bounds of the geometric spread) of less than 1.5 MPa and is computed from a subset of at least five events.

Table 2b. Characteristic Apparent Stresses τ_c for Those Seismic Regions and Faulting Types Which Had an Average Apparent Stress With a 95% Width of ≤ 1.5 MPa

	τ_c , MPa	Width, $\times 10$	Number of Events
Thrust-fault earthquakes			
Alaska-Aleutian arc	0.23	0.35	15
Northern and central Chile	0.31	0.27	15
Middle America	0.28	0.60	8
Northern Peru-Ecuador	0.42	0.38	8
Kurils	0.14	0.36	16
Eastern Coast of Honshu	0.38	0.43	19
Philippines	0.25	0.47	16
Taiwan	0.31	0.18	5
Vanuatu	0.33	0.38	15
Solomon Islands	0.33	0.38	7
Tonga-Samoa	0.26	0.60	10
Kermadec	0.15	0.52	9
Australia	0.47	0.32	6
Eastern North America	0.47	0.29	4
Central and southern California	0.87	0.20	5
Normal-fault earthquakes			
East African rift zone	0.24	0.59	9

The number of earthquakes used for each region is given. Except for eastern North America, we also required that each region have a minimum of five earthquakes before computing a τ_c .

off the east coast of Honshu and 0.42 MPa for the Peru-Ecuador region.

Not all seismic regions had a characteristic apparent stress. In some regions the seismic activity during the time interval of our study was insufficient to compute a significant $\bar{\tau}_a$. These include the Kamchatka, Marianas, and Ryukyu regions. However, the absolute spreads in apparent stress for some regions which had no dearth of activity still exceeded our criterion for designating a characteristic apparent stress. In particular, the absolute spread for the belt of seismicity encompassed roughly by New Guinea, Sulawesi, and Timor ranges from 2.5 to 4.5 MPa. These regions, however, also encompass the juncture of four major plates, suggesting that the wide spread about apparent stress arises from intense and rapid lateral variations in tectonic activity. As new data for these regions become available, the scatter about $\bar{\tau}_a$ might be reduced by decomposing the seismic regions into smaller tectonic units.

Intraplate continental. Because intraplate continental earthquakes are rare, we analyze the subset of intraplate continental earthquakes as a whole rather than by seismic region. The data set consists of 21 events, including a complement of 11 events predating November 1986 taken from *Boatwright and Choy* [1989]. The majority of events occurred in the North American and Australian cratons; seven events occurred in parts of Eurasia and Africa. As seen in Figure 8a, the absolute spread about $\bar{\tau}_a$ for intraplate earthquakes is very narrow (<1.5 MPa). Consequently, it is possible to define a characteristic apparent stress for a subset consisting of earthquakes occurring at diverse locations but a similar tectonic setting. For continental intraplate earthquakes, τ_c is 0.46 MPa, which is distinctly higher than the average value of 0.29 MPa for subduction zone earthquakes.

Near-plate margin. We categorize as near-plate marginal those earthquakes that occur near, but not on, major plate boundaries. The data set consists of 10 events. As the absolute spread about the average apparent stress is <1.5 MPa, the

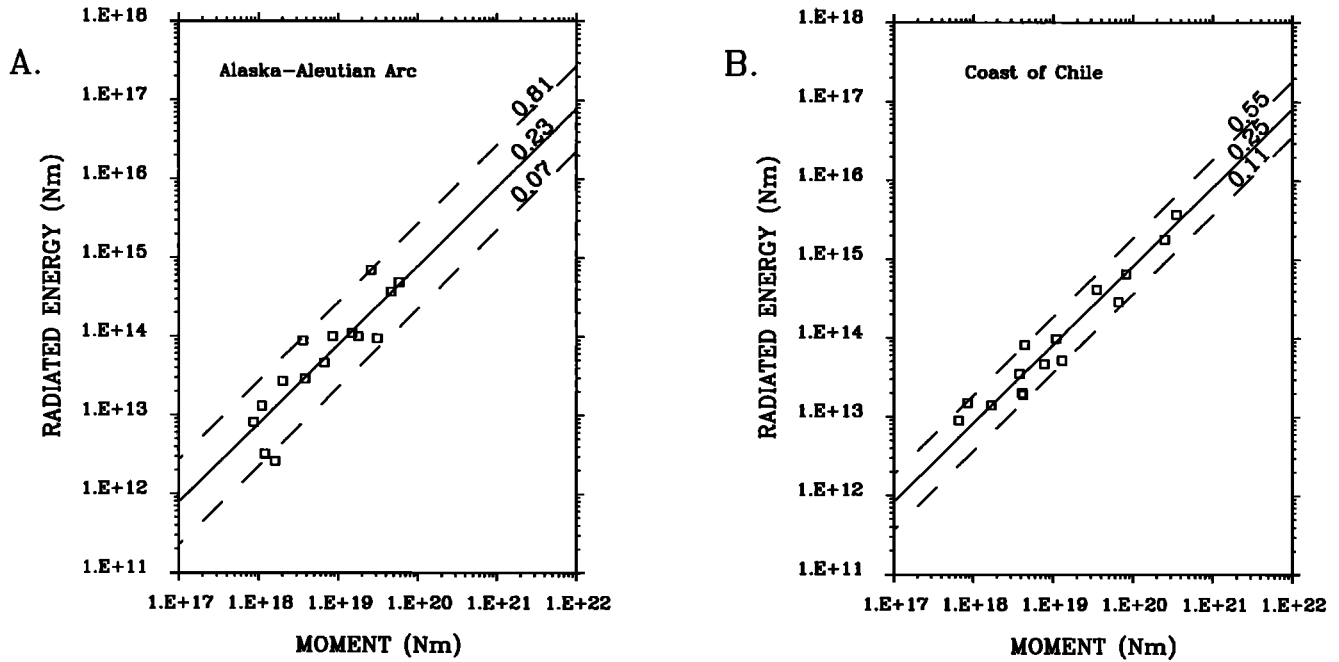


Figure 7. Regions whose earthquakes yield a small geometric spread about the average apparent stress are said to have characteristic apparent stresses (τ_c). (a) Examples are E_S - M_0 plot of thrust-fault earthquakes of the Alaska-Aleutian arc. The regression line for average apparent stress (in megapascals) and the 95% geometric spread are given by solid and dashed lines, respectively. (b) E_S - M_0 for thrust-fault earthquakes off the coast of central Chile.

earthquakes at near-plate margins have τ_c of 0.95 MPa (Figure 8b). Interestingly, two major subsets in this category also have small absolute spreads and therefore have virtually the same characteristic apparent stress as the parent data set. One group, consisting of five thrust earthquakes that occurred in

the vicinity of active oceanic ridge-transform faults, has τ_c of 1.02 MPa. The τ_c of another group of four thrust events in central and southern California is 0.87 MPa. Of all tectonic environments for which we examined thrust-faulting earthquakes, the near-plate margin has the highest τ_c .

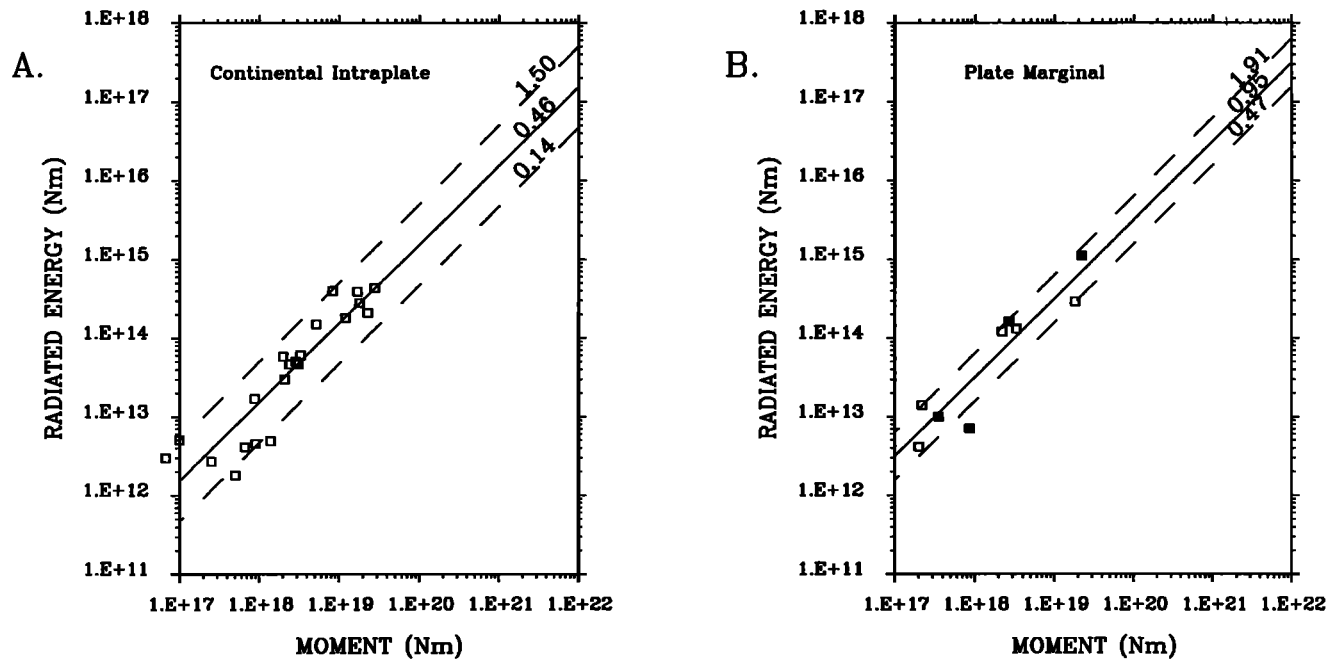


Figure 8. Subsets of earthquakes at diverse locations but similar tectonic setting can also have a characteristic apparent stress. (a) Examples are continental intraplate thrust earthquakes and (b) thrust earthquakes at near-plate margins. Solid symbols are earthquakes that occurred in central and southern California.

Continental collision. Events we categorize as continental collision are the manifestations of the collision between the Australian and Eurasian plates. We include the diffuse seismicity found in the Tibetan Platform, the adjacent South China Platform and Central China Fold System, as well as the seismicity in the Alpide belt from the Caucasus to Burma. The $\bar{\tau}_a$ for 17 continental collision thrust-fault events is 0.43 MPa. The $\bar{\tau}_a$ of earthquakes under continental collision is thus higher than under oceanic subduction. However, the large absolute spread about $\bar{\tau}_a$ for continental collision precludes us from assigning characteristic value for the environment.

Normal-Fault Earthquakes

The global energy release between 1986 and 1991 of shallow earthquakes with predominantly normal-fault mechanisms is shown in Figure 6b. The data set, consisting of 69 normal-fault earthquakes, is geographically much more sparse than the population of thrust-fault earthquakes. Only two seismic regions have the minimum of five earthquakes needed to derive a meaningful $\bar{\tau}_a$. Thus our discussion focuses more on the characteristics of normal-fault earthquakes as a function of tectonic environment rather than by seismic region. The resulting apparent stresses are summarized in Table 2.

Oceanic subduction zones. The average apparent stress for 45 normal-fault earthquakes that occurred in regions of oceanic subduction is 0.59 MPa. This is twice as high as the $\bar{\tau}_a$ of 0.29 MPa that characterizes thrust-fault earthquakes in the same environment. Inferences about the relationship between apparent stresses of normal and thrust earthquakes might appear tenuous because of the overlap in the geometric spread of apparent stress for the normal and thrust populations (2.3 and 5.6 MPa, respectively). Nevertheless, in a region by region comparison, the average apparent stress for normal-fault earthquakes remains systematically higher than those for thrust earthquakes by a factor of 2–4. An example is shown for the Alaska-Aleutian arc (Figure 9a), the only seismic region in a subduction zone with a sufficient number of normal fault earthquakes to compute an average apparent stress. The $\bar{\tau}_a$ of normal-fault events, 0.87 MPa, exceeds that of thrust-fault events, 0.23 MPa. The absolute spread of 2.0 MPa, however, exceeds our definition for a characteristic apparent stress. The only seismic region where $\bar{\tau}_a$ of thrust-fault earthquakes exceed that of normal-fault earthquakes is the trench in the Peru-Ecuador region. However, the epicenters of the thrust earthquakes are in the northern segment of the trench while the normal earthquakes are located in the southern segment of the trench. This suggests that the trench in the Peru-Ecuador region might be composed of two subregions with different regional stress fields.

Continental collision. Our data set for this tectonic environment consists of six normal-fault earthquakes. The $\bar{\tau}_a$, 0.46 MPa, is comparable to the 0.43 MPa for thrust-fault earthquakes. Both types of mechanisms have nearly the same wide geometrical spread of about 2.5 MPa.

Intraplate. The data set consists of five events, including the October 1983 Borah Peak earthquake [Boatwright and Choy, 1986]. The absolute spread about the regression line for intraplate earthquakes is much less than 1.5 MPa. For intraplate normal earthquakes, the characteristic apparent stress is 0.95 MPa, which is higher than the characteristic value of 0.46 MPa for intraplate thrust earthquakes.

Rift zones. The $\bar{\tau}_a$ for 17 normal-fault events occurring at rift environments is 0.25 MPa. The data set consists of seven

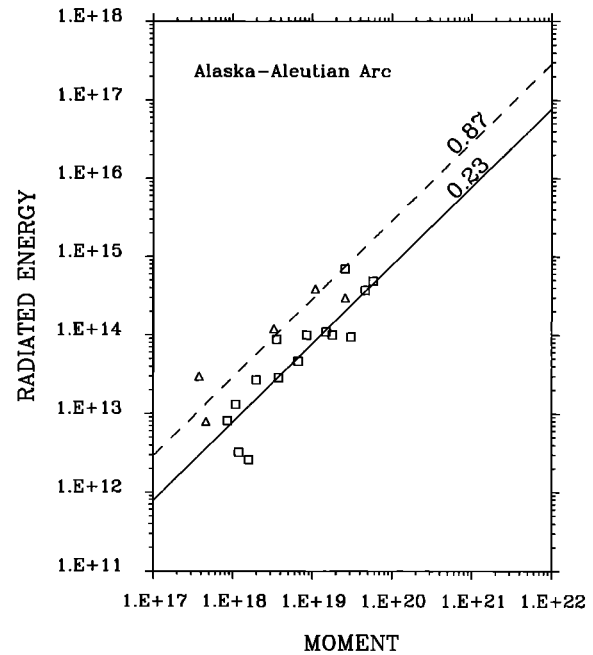


Figure 9. Thrust-fault (squares) and normal-fault (triangles) earthquakes in the Alaska-Aleutian arc. Average apparent stresses given by solid and dashed lines, respectively. In general, the average apparent stress of normal-fault earthquakes is systematically larger than that of thrust-fault earthquakes on a region by region basis for subduction zone environments.

events at oceanic ridges and 10 events that occurred about the East African rift zone. The absolute spread is less than 1.0 MPa, so 0.25 MPa is the τ_c for both oceanic and cratonic rift environments. At or near rift zones the τ_c is 4 times smaller for normal events than for thrust events. The relative difference in τ_a may arise from the different nature of the forces causing the two types of failure. Seafloor spreading probably extends down to the seismogenic zone. Thus regions of seafloor spreading are already predisposed to normal failure.

Strike-Slip Earthquakes

From the E_S - M_0 plots of Figure 5, we previously found a strong suggestion that the energy radiated by strike-slip earthquakes could be significantly different from that radiated by dip-slip earthquakes. For instance, the $\bar{\tau}_a$ for the global population of strike-slip earthquakes is 3.62 MPa, while the global averages for thrust- and normal-fault earthquakes are 0.31 and 0.48 MPa, respectively. In this section we delineate further the variations of apparent stress for earthquakes with predominantly strike-slip mechanisms by examining subsets of earthquakes as a function of tectonic environment. The global energy release of 51 shallow strike-slip earthquakes that occurred between 1986 and 1991 are plotted in Figure 6c. The $\bar{\tau}_a$ as a function of tectonic setting are summarized in Table 2a.

Oceanic ridge-ridge transform faults. The $\bar{\tau}_a$ for 13 strike-slip earthquakes that occurred at mid-oceanic transform faults is 4.48 MPa (Figure 10a). This is about an order of magnitude higher than the average apparent stresses of normal and thrust earthquakes in the vicinity of mid-oceanic ridges and transforms, which are 0.25 and 1.02 MPa, respectively. High apparent stresses would imply that the rupture of oceanic transforms requires commensurately high stress drops. Alternatively, high

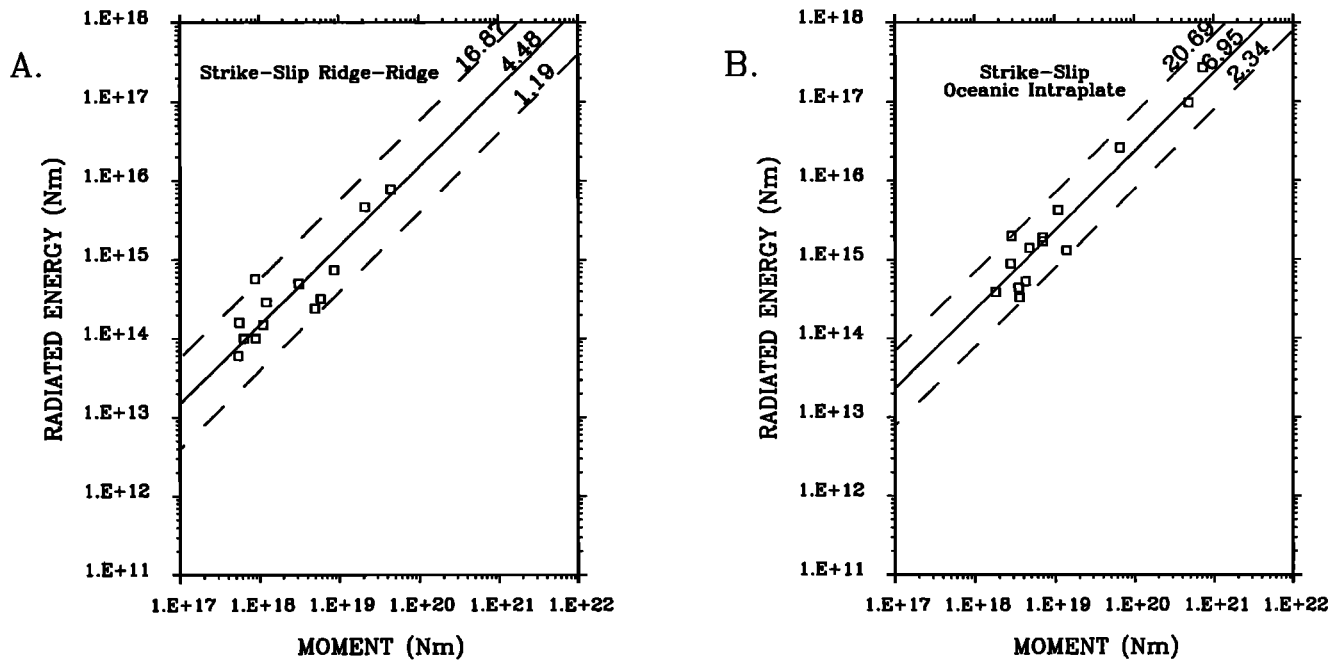


Figure 10. (a) E_S - M_0 plots for strike-slip faulting earthquakes at oceanic ridge-ridge transform faults. (b) E_S - M_0 plots for strike-slip earthquakes in oceanic intraplate settings. The average apparent stresses for these two classes of earthquakes are 4.48 and 6.95 MPa, respectively, which are the highest for any combination of fault type and tectonic setting in the world.

values of apparent stress can arise if the moment used in its computation is underestimated. In a search for slow earthquakes, *Beroza and Jordan* [1990], using free oscillation data, found that the majority of slow earthquakes occurring in 1978–1979 were associated with oceanic transform faults. *Beroza and Jordan* [1990] also applied the total-moment spectral technique of *Silver and Jordan* [1983] to derive the total-scalar moment of the transform earthquakes. The technique had been used by *Silver and Jordan* [1983] to detect strong frequency dependence in moment for dip-slip earthquakes. Their total-scalar moments for seven of eight slow earthquakes along transform faults were not significantly different (by less than 20%) from the centroid moment. Only one earthquake had a total-scalar moment that was substantially higher (by a factor of 3) than the centroid moment. High apparent stress for most oceanic transform faults is probably not an artifact of underestimating total moment; it is a physical attribute of oceanic transform earthquakes. Furthermore, any slow component of rupture in large thrust earthquakes would reduce the estimate of apparent stress. The effect of larger moment would only widen the separation in apparent stress between strike-slip and thrust earthquakes.

Oceanic intraplate earthquakes. The combination of tectonic environment and faulting type that produced the highest average apparent stress is found in the set of strike-slip earthquakes located within oceanic plate boundaries. The average apparent stress for 16 intraplate oceanic earthquakes is 6.95 MPa (Figure 10b). Ten of these earthquakes occurred 1° or 2° seaward of the trench axis of an island arc. Six events occurred behind an interplate boundary where strike-slip faults have developed to accommodate oblique convergence at a tightly coupled subduction interface. The arc structure in the vicinity of these events is nearly always nonlinear. Examples, as illus-

trated in Figure 11, are the unusually large intraplate earthquakes in the Gulf of Alaska on November 30, 1987, and March 6, 1988, and also events seaward of the Ryukyu Trench between the Nankai Trough and the Izu-Bonin Trench. The nonlinear concavity characterizing each of these island arcs implies that the direction of convergence between the oceanic plate and the island arc has a strong oblique component. *Lahr et al.* [1988] for the Gulf of Alaska earthquakes and *Chamot-Rooke and LePichon* [1989] for the Ryukyu Trench-Nankai Trough region have shown that strong lateral compressive stresses can thus arise that are conducive to strike-slip failure.

Transitional boundaries. A transitional boundary is one in which contemporary transform plate motion is evolving into or from a state of convergence or divergence. The apparent stress for the data set of seven transitional earthquakes is between 1.0 and 3.0 MPa. We term this range of apparent stress as intermediate. It is from 2–4 times greater than the average apparent stress of subduction-zone thrust events but about one-half of the high apparent stresses of strike-slip events at oceanic intraplate and ridge-ridge transforms.

Two such earthquakes occurred in oceanic settings. The Komandorsky Islands earthquake of May 1989 occurred just north of the cusp of the Kuril-Kamchatka and Aleutian arcs which marks the change from underthrusting to strike-slip faulting. It had an apparent stress of 1.9 MPa. The location of the Macquarie Ridge earthquake of May 1989 earthquake is on a transform fault between two zones of convergence. It is regarded as the site of incipient trench formation [*Ruff et al.*, 1989; *Mueller and Phillips*, 1991]. The earthquake had an apparent stress of 2.08 MPa.

Five other events occurred in two types of intracontinental settings. The first setting involves strike-slip faults on laterally moving shear belts bounding blocks of crust that were formed

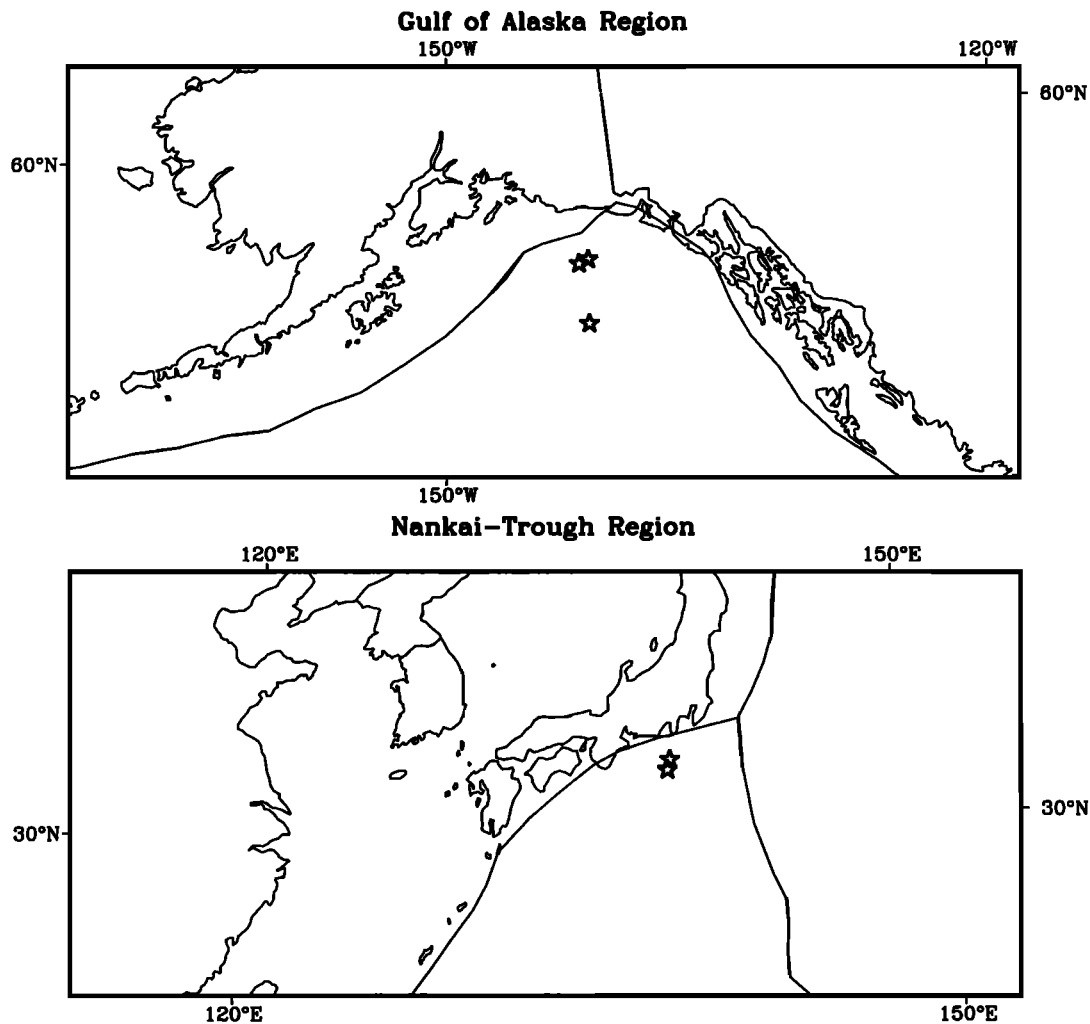


Figure 11. Two types of nonlinear arc geometry in which oceanic intraplate earthquakes with strike-slip mechanisms occur. (top) Broad concave arcs as exemplified by the Aleutian arc. The stars indicate locations of three large intraplate earthquakes in the Gulf of Alaska in 1988 and 1989. (bottom) Acute concave arcs as represented by the sharply deformed Ryukyu trench. The stars indicate locations of two large intraplate earthquakes seaward of the trench that occurred in 1990 and 1991. In both geometries, strong lateral compressive forces arise to fragment crustal material.

in response to continental collision. Three events in central Asia, including the destructive earthquake of June 1990 in Iran, compose our data set of strike-slip events in zones of continental collision. Their average apparent stress is 1.35 MPa. Two strike-slip events occurred in predominantly extensional continental environments. The average apparent stress for an earthquake in the Gulf of California and another in Sudan is 1.23 MPa. Generally, the apparent stress of strike-slip events exceeds the apparent stress of dip-slip earthquakes when both occur in the same seismic region. For instance, the Sudan earthquake of May 1990 was followed by three large normal-fault aftershocks ($m_b > 5.8$) which had an average apparent stress of 0.20 MPa.

The Macquarie Ridge earthquake also provides one more opportunity to look for frequency-dependent moment in strike-slip earthquakes. By any measure of earthquake size (Tables 3 and 4) the Macquarie Ridge earthquake ranks as one of the three largest earthquakes that occurred between 1986 and 1991. Frequency-dependent moment, if it were significant,

would certainly have been manifested by this earthquake. The moments from both centroid moment tensor and body wave analyses [Braunmüller and Nábělek, 1990; Tichelaar and Ruff, 1990] range from 1.4 to 1.8×10^{21} N m. Moments from surface wave analyses [Ekström and Romanowicz, 1990; Satake and Kanamori, 1990] averaged about 2.0×10^{21} N m. The lowest-frequency estimate of moment, derived from an inversion of normal mode data [Park, 1990], was also 2.0×10^{21} N m. The range of estimates, from 1.4 to 2.0×10^{21} N m, is small and consistent with the earlier observation that the most oceanic strike-slip earthquakes did not exhibit significant frequency-dependent moment.

Discussion

Relationship of Energy to Magnitude and Moment

The logarithmic magnitude scale devised by Gutenberg and Richter has been a successful technique for the ranking of relative earthquake size. Unfortunately, the use of M_S has

Table 3. Twenty Largest Earthquakes Between 1986 and 1991 Ranked by Energy in Terms of M_E

Rank	Region	Date	FM	M_E	M_W	M_S
1	Gulf of Alaska (T, 85 cm)	Nov. 30, 1987	SS	8.42	7.91	7.6
2	Macquarie Islands Region (T)	May 23, 1989	SS	8.12	8.10	8.2
3	Gulf of Alaska (T, 10 cm)	March 6, 1988	SS	8.12	7.79	7.6
4	Gulf of Alaska (T, 10 cm)	Nov. 17, 1987	SS	7.74	7.21	6.9
5	Luzon, Philippine Islands	July 16, 1990	SS	7.65	7.74	7.8
6	Western Iran	June 20, 1990	SS	7.49	7.43	7.7
7	Off Coast of northern California (T, 50 cm)	Aug. 17, 1991	SS	7.39	7.10	7.1
8	Aroe Islands region (T)	July 25, 1988	NR	7.35	6.96	6.7
9	Tonga Islands region	Oct. 6, 1987	NR	7.26	7.30	7.3
10	Off coast of Oregon	July 13, 1991	SS	7.24	6.88	6.9
11	Mariana Islands region (T, 24 cm)	April 5, 1990	NR	7.23	7.47	7.5
12	Tonga Islands (T, 25 cm)	April 6, 1991	SS	7.22	6.69	6.7
13	Costa Rica (T, 2 m)	April 22, 1991	TH	7.14	7.68	7.6
14	Burma-China border region	Nov. 6, 1988	SS	7.13	7.05	7.3
15	East Papua New Guinea region	Feb. 8, 1987	SS	7.04	7.36	7.4
16	Banda Sea	June 17, 1987	TH	7.03	7.12	—
17	South of Fiji Islands	Aug. 14, 1989	SS	7.00	6.31	5.9
18	Macquarie Islands region	Sept. 17, 1990	SS	7.00	6.44	6.0
19	Molucca Passage	Feb. 10, 1989	TH	6.99	7.15	6.8
20	Near coast of northern Chile (T, 22 cm)	March 5, 1987	TH	6.97	7.60	7.3

The associated M_S and M_W are also given. Three significant digits are used in M_E and M_W in order to refine the ranking. The type of faulting mechanism (FM) is indicated by TH (thrust), NR (normal), and SS (strike-slip). T indicates a tsunami was generated; a wave height, if reported, is also given.

inadequacies that have long been recognized [e.g., *Hanks and Thatcher, 1972*]. For very large earthquakes or very deep earthquakes the single frequency used to compute M_S is no longer representative of the dimensions of the earthquake. To circumvent this limitation, we can reverse the normal usage of (5). Previously, E_S was derived from M_S . Because E_S is now explicitly computed, we can define an energy magnitude by simply solving (5) for magnitude,

$$M_E = (\log E_S - a)/b, \quad (9)$$

where M_S has been renamed M_E as it is now measured from velocity power spectra rather than an amplitude at a certain frequency. We have shown that on average the constants of the original Gutenberg-Richter formula slightly overestimate energy. A more accurate relationship can be derived from (6). However, if we are concerned with relative rather than absolute size of earthquakes, the choice of constants is only a technicality. For consistency with historical computations as well as with other types of magnitude that have been derived

Table 4. Twenty Largest Earthquakes Between 1986 and 1991 Ranked by Moment in Terms of M_W

Rank	Region	Date	FM	M_E	M_W	M_S
1 (1)	Macquarie Islands (T)	May 23, 1989	SS	8.12	8.10	8.2
2 (5)	Gulf of Alaska (T, 85 cm)	Nov. 30, 1987	SS	8.42	7.91	7.6
3 (5)	Gulf of Alaska (T, 10 cm)	March 6, 1988	SS	8.12	7.79	7.6
4 (2)	Luzon, Philippines	July 16, 1990	SS	7.65	7.74	7.8
5 (9)	Sulawesi	April 18, 1990	TH	6.90	7.68	7.4
6 (5)	Costa Rica (T, 2 m)	April 22, 1991	TH	7.14	7.68	7.6
7 (9)	South of Fiji	March 3, 1990	SS	6.95	7.65	7.4
8 (9)	Kuril Islands	Dec. 22, 1991	TH	6.61	7.63	7.4
9 (16)	Coast of northern Chile (T, 22 cm)	March 5, 1987	TH	6.97	7.60	7.3
10 (9)	Solomon Islands	Aug. 10, 1988	TH	6.50	7.60	7.4
11 (16)	Mindanao, Philippines	Dec. 15, 1989	TH	6.64	7.59	7.3
12 (25)	Sulawesi	June 20, 1991	TH	6.45	7.57	7.0
13 (8)	Mariana Islands (T, 24 cm)	April 5, 1990	NR	7.23	7.47	7.5
14 (16)	Macquarie Islands	Sept. 3, 1987	NR	6.76	7.43	7.3
15 (9)	East coast of Honshu (T, 56 cm)	Nov. 1, 1989	TH	6.85	7.43	7.4
16 (4)	Western Iran	June 20, 1990	SS	7.49	7.43	7.7
17 (9)	New Britain (T, 13 cm)	Oct. 16, 1987	TH	6.37	7.41	7.4
18 (2)	Taiwan	Nov. 14, 1986	TH	6.94	7.41	7.8
19 (9)	Eastern Papua New Guinea	Feb. 8, 1987	SS	7.04	7.36	7.4
20 (25)	Costa Rica	March 25, 1990	TH	6.36	7.36	7.0

The rank of the same event by M_S , which is rounded off to two significant digits, is given in parentheses. The associated M_E is given. The type of faulting mechanism (FM) is indicated by TH (thrust), NR (normal), and SS (strike-slip). T indicates a tsunami was generated; a wave height, if reported, is also given.

from the Gutenberg-Richter formula, we retain the original constants. Thus, in units of Newton meters,

$$M_E = 2/3 \log E_S - 3.2. \quad (10)$$

The advantages of (10) are that (1) a magnitude is definable as long an energy can be computed; (2) the definition is based on the traditional formula for M_S ; and (3) there is still a mapping from the M_E back to energy.

An important form of (10) results when we express E_S in terms of M_0 . Combining (8) and (10),

$$M_E = 2/3 [\log M_0 + \log (\tau_a/\mu)] - 3.2. \quad (11)$$

Equation (11) implies that energy magnitude, as well as energy itself, can be estimated for an historical earthquake if the moment is known and if the earthquake occurs in a seismic region for which a characteristic apparent stress τ_c is known. In contrast to energy, M_0 for historical earthquakes can be derived in numerous ways not requiring spectral analysis. Thus, for instance, M_0 has been estimated from surface faulting, preseismic and postseismic geodetic and geological data, and the spatial distribution of aftershocks. Furthermore, as statistics about radiated energy and apparent stress are accumulated, the τ_c for regions in addition to those of Table 2 can be delineated and refined. As the global variations between energy and moment become more precise, they can be applied to improving the worldwide estimation of seismic hazard potential from historical data.

Finally, we compare M_E to other measures of earthquake size, such as M_W . Because M_E is, in general, unequal to M_W , it is important to understand the extent and physical nature of the difference. We note that (11) reduces to the definition of moment magnitude, M_W , under the condition $E_S/M_0 \approx 5 \times 10^{-5}$ as used by Kanamori [1977],

$$M_E = 2/3 \log M_0 - 6.0 = M_W. \quad (12)$$

Kanamori's E_S/M_0 value comes from assuming that stress drop is between 2.0 and 6.0 MPa. An equivalent interpretation of this value, however, is that it is equivalent to $\tau_a \approx 5 \times 10^{-5} \mu$. For shallow earthquakes, where $\mu \approx 0.3 - 0.6 \times 10^5$ MPa, this condition implies that M_E and M_W will be coincident only for earthquakes with apparent stresses in the range 1.5–3.0 MPa. From Table 2a, we can group characteristic apparent stresses τ_c into three levels: low (between 0.0 and 1.5 MPa), intermediate (from 1.5 to 3.0 MPa) and high (greater than 3.0 MPa). The majority of global thrust-fault earthquakes fall into the low category, whereas the majority of global strike-slip earthquakes fall into the high category. M_W will generally be larger than M_E for most thrust-fault earthquakes; it will be smaller than M_E for most strike-slip earthquakes. The inconsistency arises from the assumption in the computation of M_W that τ_a/μ is a fixed ratio. We have shown that apparent stress is, in fact, strongly affected by focal mechanism and tectonic environment. Our definition of M_E follows the original intent of the Gutenberg-Richter formula by relating energy to magnitude. In addition, M_E does not impose an a priori value of apparent stress.

In Tables 3 and 4, we list the 20 largest shallow earthquakes that occurred between November 1986 to December 1991 as ranked by M_E , M_W , and M_S . Only eight earthquakes are common to all lists, which is not surprising since each of the

magnitudes emphasizes a different aspect of the rupture process. When earthquake size is ranked by energy (M_E), the list of the largest events is dominated by strike-slip earthquakes. When earthquake size is ranked by moment (M_W), the list of the largest events is dominated by thrust-fault earthquakes. Two large strike-slip earthquakes off the western coast of the United States, for example, are ranked seventh and tenth by energy but are ranked 36th and 55th by moment. Thus, if seismic hazard is related to earthquake size, then it is important to note that the potential for damage predicted by energy, moment, and M_S are different. A second feature seen in the ranking by M_E is that tsunamis were generated by five of the large oceanic strike-slip earthquakes. In contrast, tsunamis were generated by only one thrust-fault and two normal-fault earthquakes. The efficiency of tsunamigenesis may be related to the strike-slip rupture process itself, to an associated strong component of dip slip, or to the triggering of secondary faults. Energy as an independently computed source parameter can complement moment and magnitude both as a measure of earthquake size and for evaluating tsunamigenic potential.

Relationships of Apparent Stress to Faulting Type and Tectonic Environment

A compelling reason for the direct computation of energy is that empirical formulas by definition suppress significant regional and tectonic variations in energy release. In tandem with moment, estimates of energy yield the apparent stress of an earthquake. In contrast to the plot of E_S-M_0 for the worldwide population of earthquakes, subsets of data often exhibit such small scatter that a characteristic apparent stress τ_c can be associated with various combinations of faulting mechanism and tectonic setting. The hierarchy of average apparent stresses (Table 2a) can be systematically related to tectonic forces active in different settings. For convenience, we group average apparent stress into three levels: low ($\tau_a < 1.0$ –1.5 MPa), intermediate (1.0 –1.5 $< \tau_a < 3.0$ MPa), and high ($\tau_a > 3.0$ MPa). The τ_a for most subsets of dip-slip earthquakes fall into the low category, while the τ_a for most subsets of strike-slip earthquakes fall in the intermediate or high range.

The dominant mode of failure for a tectonic environment is associated with the faulting type having the lowest average apparent stress. By examining seismic regions in which both normal and thrust earthquakes have occurred, we are able to discern systematic relationships between the two types of faulting as a function of tectonic setting. For oceanic ridges the τ_a of normal-fault earthquakes (0.25 MPa) is considerably lower than that of thrust earthquakes (0.62 MPa). The situation is reversed at oceanic subduction zones. The apparent stress of normal-fault earthquakes generally exceeds that of thrust-fault earthquakes in any given seismic region. In other words, near subduction zones, thrust-fault earthquakes are characterized by the lowest average apparent stress. Near oceanic spreading centers, normal-fault earthquakes exhibit the lowest apparent stress.

Within a given tectonic setting and faulting type, seismic regions can have their own characteristic apparent stress τ_c . For instance, the average apparent stress is $\bar{\tau}_a$ 0.29 MPa for the composite of all oceanic subduction zone earthquakes. However, the τ_c for individual seismic regions may range from 0.15 to 0.42 MPa. The variation in τ_c among seismic regions suggests that moment and energy release may be affected by

regional differences in properties of the subducting plate, such as its age, dip, or size of interplate asperities. In contrast, the τ_c for intraplate continental earthquakes, 0.46 MPa, is slightly but systematically higher than the $\bar{\tau}_a$ of subduction zone events. This suggests that the stresses associated with intraplate ruptures, whether caused by reactivation of old preexisting faults or by fracture of fresh rock, are higher than stresses associated with ruptures at a plate interface. Although this hypothesis is not new [e.g., *Kanamori and Allen, 1986*], it can now be supported by direct computation of source parameters. In addition, the narrow geometric spread in apparent stress for intraplate earthquakes suggests that there is some commonality in their mechanism that is relatively independent of worldwide variations in geology. *Boatwright and Choy [1989]* have noted that large intraplate earthquakes share two general rupture characteristics: shallow depths of nucleation (on average about 5 km) and small rupture radii (limited to about ≤ 7 km). These characteristics may be attributed to the seismogenic thickness of intraplate regimes, which is constrained by the depth at which aseismic deformation occurs in the middle and lower continental crust. The limitation on seismogenic thickness may also constrain the amount of stress that can accumulate in continental crust.

The hierarchy of apparent stresses near subducting plate margins may be indicative of the influence of the fabric of a plate, as determined by the orientation of a spreading ridge, in the buildup of stresses and stress release. Near subducting margins, preexisting planes of weakness exist which were originally created during normal faulting in the near-ridge environment. The ruptures with the highest apparent stress are strike-slip earthquakes in oceanic intraplate regions. The apparent stresses may be high because the earthquakes occur where the existing lateral stresses are not properly oriented to utilize these preexisting planes of weakness. On the other hand, plate-bending forces just seaward of a plate interface may preferentially reactivate these planes of weakness. Because of the favorable orientation of the fault planes, the apparent stress of the resulting normal-fault earthquakes would be substantially lower than that of intraplate strike-slip earthquakes. Finally, in contrast to normal-fault earthquakes that may occur on a reactivated fault, subduction zone thrust earthquakes occur at plate interfaces which are often the site of repeated slip. The apparent stresses will be low because failure occurs on segments of plate boundary which are strain weakened by the continuous occurrence of thrust earthquakes.

Intermediate apparent stresses are associated with strike-slip earthquakes at interplate boundaries which are in transition from one type of plate motion to another. This level is from 2 to 4 times greater than the average apparent stress of subduction zone thrust events but about one-half the average apparent stress of oceanic intraplate strike-slip events. This suggests that the strength at zones of transitional plate boundaries is between that of a fully developed plate interface (where fracture may occur on preexisting zones of weakness) and that of a region internal to the plate (where preexisting zones of weakness are not likely to exist).

Finally, the highest apparent stresses of any tectonic environment and faulting type are found for strike-slip earthquakes at oceanic intraplate sites and at oceanic ridge-ridge transforms. If the high apparent stresses are not an artifact of frequency-dependent moment, the stress drops for these

strike-slip earthquakes must be commensurately high. Strike-slip earthquakes at oceanic intraplate settings occur in crustal material which had been migrating basically unperturbed since its formation at a spreading ridge. The high apparent stress of intraplate earthquakes suggests that high stress drops are required to fragment relatively cold and intact crustal material. In contrast, as we noted before, the low apparent stress of thrust earthquakes at island arcs suggests that lower stress drops are needed to rupture plate interfaces that are weakened by the repeated occurrence of earthquakes during subduction.

Our results also imply commensurately high stress drops for strike-slip earthquakes at oceanic ridge-ridge transforms. Although many analyses of oceanic ridge-ridge transforms conclude that transform boundaries are weak relative to surrounding oceanic lithosphere, the actual strength remains controversial (e.g., see the review by *Bergman and Solomon [1992]*). Stresses required to rupture a transform fault surface may be elevated by nonfrictional factors such as thermal annealing [*Severinghaus and Macdonald, 1989*]. Established transform faults acting to resist changes in relative plate motion may also be result in strong compressional forces [*Richards and Engebretson, 1994*].

Conclusions

There are two compelling reasons for computing seismic energy directly. First, we have shown that radiated energy gives a physically different measure of earthquake size than seismic moment. Energy is derived from the velocity power spectra, while moment is derived from the low-frequency asymptote of the displacement spectra. Thus energy is a measure of seismic potential for damage, while moment, being related to the final static displacement, is more related to the long-term tectonic implication of an earthquake. The second major reason for the direct computation of energy is that significant regional and tectonic variations in energy release are suppressed by empirical formulas. Impediments to the direct and routine computation of radiated energy of teleseismically recorded earthquakes have been largely removed by the deployment of many global networks that record data digitally over a broad bandwidth. The radiated energies for 397 earthquakes are listed in Table 5. Systematic variations in the release of energy and apparent stress as a function of faulting type and tectonic setting can now be identified that were previously undetectable because of the lack of reliable energy estimates. The geometric spread about the average apparent stress for many seismic regions or tectonic environments is often so narrow that a characteristic apparent stress τ_c can be associated with them. Characterizing the level of apparent stress associated with classes of earthquakes having particular faulting types and occurring in particular tectonic settings may provide new insight into the state of stress in the Earth's crust. Events with anomalous apparent stresses will be easier to distinguish as more data are accumulated and baselines for τ_c more refined. An energy magnitude M_E , derived from an independent computation of energy, can complement M_W and M_S in estimating seismic and tsunamigenic potential. As the global correlations between energy and moment become more precise, they can be applied to improving the estimation of seismic hazard potential both on a near-real-time basis and for historical earthquakes.

Table 5. Radiated Energies and Seismic Moments

No.	Origin		Latitude, deg	Longitude, deg	m_b	M_S	E_S , N m	M_0 , N m	τ_a	θ , deg	δ , deg	λ , deg	Reference
	Date	Time											
<i>Alaska-Aleutian Arc</i>													
1	Jan. 5, 1987	1211:55.8	52.45	-169.38	6.1	6.7	0.11E+15	0.15E+20	2.2	246	26	95	C
2	Feb. 27, 1987	0831:54.4	53.47	-167.29	6.2	6.7	0.30E+15	0.26E+20	3.5	185	73	270	F
3	March 22, 1987	0249:15.9	51.59	-173.57	5.9	6.0	0.27E+14	0.20E+19	4.0	256	25	103	C
4	May 6, 1987	0406:14.1	51.27	-179.90	6.3	6.4	0.10E+15	0.85E+19	3.5	293	56	148	M
5	June 21, 1987	0546:10.0	54.21	-162.60	6.2	6.2	0.46E+14	0.67E+19	2.1	240	18	90	F
6	July 10, 1987	1849:53.9	55.14	165.52	6.1	6.3	0.88E+14	0.36E+19	7.3	120	77	160	F
7	Nov. 17, 1987	0846:53.3	58.59	-143.27	6.6	6.9	0.26E+17	0.66E+20	118.2	184	88	173	F
8	Nov. 30, 1987	1923:19.6	58.68	-142.79	6.7	7.6	0.27E+18	0.73E+21	111.0	262	87	0	F
9	Feb. 7, 1988	1815:05.6	50.78	173.46	6.2	6.0	0.12E+15	0.33E+19	10.9	213	67	338	M
10	Feb. 16, 1988	0422:36.2	51.56	175.04	5.9	5.7	0.13E+14	0.11E+19	3.5	275	12	107	C
11	Feb. 29, 1988	0531:41.5	55.15	167.43	6.1	6.8	0.70E+15	0.26E+20	8.1	131	56	187	C
12	March 6, 1988	2235:38.1	56.95	-143.03	6.8	7.6	0.97E+17	0.49E+21	59.4	61	79	358	F
13	Nov. 15, 1988	0841:42.3	52.11	-171.10	5.9	5.4	0.81E+13	0.86E+18	2.8	230	26	78	C
14	May 24, 1989	1331:14.5	56.18	164.26	5.9	6.1	0.44E+15	0.35E+19	37.7	18	80	7	C
15	June 16, 1989	1051:21.6	57.76	-153.99	5.8	.	0.30E+14	0.38E+18	23.7	240	85	295	F
16	Sept. 4, 1989	1314:58.3	55.54	-156.84	6.5	6.9	0.37E+15	0.46E+20	2.4	245	9	90	F
17	Oct. 7, 1989	1548:29.1	51.31	-179.03	6.1	6.7	0.10E+15	0.18E+20	1.7	266	21	113	C
18	Oct. 9, 1989	1801:07.9	51.78	171.87	6.0	5.3	0.79E+13	0.46E+18	5.2	174	27	284	C
19	March 12, 1990	1441:19.5	51.48	-175.03	6.0	6.2	0.29E+14	0.38E+19	2.3	229	21	76	C
20	May 29, 1990	1831:12.3	56.96	-153.57	5.9	5.8	0.26E+13	0.16E+19	0.5	230	13	90	F
21	Nov. 6, 1990	2014:29.7	53.45	169.87	6.3	7.0	0.49E+15	0.58E+20	2.5	166	21	27	M
22	Feb. 21, 1991	0235:34.0	58.43	-175.45	6.2	6.5	0.39E+15	0.11E+20	10.6	279	70	320	F
23	May 30, 1991	1317:42.0	54.57	-161.61	6.3	6.7	0.94E+14	0.31E+20	0.9	248	12	90	F
24	Nov. 26, 1991	1041:32.0	51.40	-176.00	5.8	5.6	0.32E+13	0.12E+19	0.8	230	25	90	F
<i>Eastern Alaska to Vancouver</i>													
25	Feb. 28, 1979	2127:06.1	60.64	-141.59	6.4	7.1	0.14E+16	0.20E+21	2.1	255	12	85	E
<i>California-Nevada Region</i>													
26	May 2, 1983	2342:47.7	36.22	-120.32	6.2	6.5	0.16E+15	0.27E+19	17.8	300	80	80	A
27	Oct. 1, 1987	1442:20.0	34.06	-118.08	5.8	5.7	0.71E+13	0.86E+18	2.5	270	48	112	F
28	Oct. 18, 1989	0004:15.2	37.04	-121.88	6.6	7.1	0.11E+16	0.22E+20	15.0	130	65	140	H
29	June 28, 1991	1443:54.5	34.26	-118.00	5.8	5.1	0.10E+14	0.35E+18	8.6	201	60	33	F
30	July 13, 1991	0250:14.7	42.18	-125.64	6.2	6.9	0.46E+16	0.21E+20	65.7	131	81	175	M
31	Aug. 16, 1991	2226:17.2	41.70	-125.39	5.5	6.3	0.50E+15	0.31E+19	48.4	310	90	185	F
32	Aug. 17, 1991	1929:40.0	40.24	-124.35	6.0	6.2	0.40E+14	0.19E+19	6.3	48	38	141	M
33	Aug. 17, 1991	2217:14.7	41.82	-125.40	6.2	7.1	0.78E+16	0.44E+20	53.2	125	87	180	F
<i>Lower California-Gulf of California</i>													
34	June 18, 1988	2249:42.4	26.86	-111.00	5.9	7.0	0.70E+15	0.11E+20	19.1	30	90	0	F
<i>Mexico-Guatemala Region</i>													
35	Oct. 25, 1981	0322:15.5	18.05	-102.08	6.2	7.3	0.79E+15	0.73E+20	3.2	286	20	82	E
36	Sept. 19, 1985	1317:47.4	18.19	-102.53	6.8	8.1	0.13E+17	0.11E+22	3.5	301	18	105	E
37	July 15, 1987	0716:13.6	17.52	-97.15	5.9	.	0.53E+13	0.26E+19	0.6	305	47	296	M
38	April 25, 1989	1429:00.5	16.77	-99.33	6.2	6.8	0.25E+15	0.24E+20	3.1	276	10	66	C
39	Aug. 29, 1989	0416:23.0	18.04	-105.67	5.7	6.6	0.77E+14	0.69E+19	3.3	193	78	5	M
40	Jan. 1, 1991	0006:31.4	18.07	-105.85	5.5	6.2	0.21E+15	0.28E+19	22.5	203	83	7	F
<i>Central America</i>													
41	April 3, 1983	0250:01.1	8.72	-83.12	6.5	7.3	0.77E+15	0.15E+21	1.5	300	30	93	E
42	Sept. 9, 1989	0140:35.8	2.43	-79.76	6.0	5.0	0.72E+12	0.42E+18	0.5	215	60	295	F
43	March 25, 1990	1316:06.9	9.81	-84.83	5.8	6.4	0.13E+14	0.00E+00	0.0	278	20	90	F
44	March 25, 1990	1322:55.6	9.92	-84.81	6.2	7.0	0.22E+15	0.11E+21	0.6	212	43	27	F
45	April 3, 1990	2257:00.9	11.43	-86.30	5.5	6.4	0.34E+14	0.18E+20	0.6	279	21	68	F
46	April 28, 1990	0123:11.5	8.89	-83.50	5.9	6.3	0.25E+14	0.42E+19	1.8	310	28	114	F
47	May 8, 1990	0001:40.0	6.91	-82.62	6.2	6.3	0.54E+15	0.58E+19	27.9	342	85	147	F
48	Dec. 17, 1990	1100:29.9	6.64	-81.93	5.7	5.9	0.55E+14	0.28E+19	5.9	263	83	345	F
49	March 5, 1991	1349:06.4	3.23	-83.34	5.9	5.5	0.18E+14	0.32E+18	16.9	45	54	39	F
50	April 4, 1991	0322:57.9	7.02	-78.15	6.1	5.8	0.59E+14	0.20E+19	8.8	302	62	25	F
51	April 22, 1991	2156:51.8	9.69	-83.07	6.3	7.6	0.32E+16	0.33E+21	2.9	292	80	121	F
52	April 24, 1991	1913:02.1	9.74	-83.52	5.6	6.1	0.39E+15	0.18E+19	65.0	145	90	175	F
<i>Caribbean Loop</i>													
53	Aug. 12, 1987	0309:59.5	14.09	-59.26	5.7	5.3	0.97E+13	0.35E+18	8.3	6	76	174	M
54	March 10, 1988	0617:23.3	10.40	-60.59	6.2	6.4	0.23E+15	0.11E+20	6.3	252	58	328	F
55	June 24, 1988	0857:53.3	10.21	-60.56	6.0	5.6	0.17E+14	0.75E+18	6.8	354	50	202	M
56	April 15, 1989	1426:41.3	8.45	-61.04	5.8	5.1	0.84E+13	0.14E+18	18.0	194	29	207	C
57	April 30, 1989	0822:54.0	10.96	-68.32	5.9	6.0	0.43E+14	0.90E+18	14.3	242	36	147	M
58	June 18, 1989	1406:28.8	17.76	-68.81	5.9	.	0.70E+13	0.18E+18	11.7	34	64	338	C

Table 5. Radiated Energies and Seismic Moments

No.	Origin		Latitude, deg	Longitude, deg	m_b	M_S	E_S , N m	M_0 , N m	τ_a	θ , deg	δ , deg	λ , deg	Reference
	Date	Time											
<i>Andean South America</i>													
59	March 3, 1985	2247:26.9	-33.12	-71.62	6.7	7.8	0.37E+16	0.35E+21	3.2	360	35	105	D
60	March 4, 1985	1501:09.2	-33.84	-71.43	6.0	6.0	0.19E+14	0.42E+19	1.4	330	30	65	D
61	March 17, 1985	1041:39.0	-32.65	-71.62	5.9	6.6	0.47E+14	0.78E+19	1.8	350	20	90	D
62	March 19, 1985	0401:08.4	-33.13	-71.64	5.9	6.6	0.52E+14	0.13E+20	1.2	355	15	100	D
63	March 25, 1985	0514:34.3	-34.20	-72.23	6.0	6.4	0.35E+14	0.38E+19	2.8	340	15	90	D
64	April 3, 1985	1306:20.4	-32.57	-71.71	5.8	6.1	0.14E+14	0.17E+19	2.5	360	15	95	D
65	April 9, 1985	0157:01.1	-34.06	-71.59	6.3	7.2	0.65E+15	0.82E+20	2.4	350	30	90	D
66	March 5, 1987	0917:05.3	-24.39	-70.16	6.5	7.3	0.18E+16	0.25E+21	2.2	12	23	106	C
67	March 6, 1987	0154:50.5	0.05	-77.65	6.1	6.1	0.27E+15	0.49E+19	16.5	233	38	152	M
68	March 6, 1987	0410:42.0	0.15	-77.82	6.5	6.9	0.65E+15	0.64E+20	3.0	353	72	90	F
69	Aug. 8, 1987	1548:56.8	-19.02	-69.99	6.4	6.9	0.19E+15	0.79E+20	0.7	149	24	257	M
70	Aug. 15, 1987	1804:23.1	-28.14	-70.88	6.0	6.1	0.81E+14	0.44E+19	5.5	20	30	110	C
71	Dec. 28, 1987	0816:21.4	-28.06	-70.61	6.1	.	0.15E+14	0.85E+18	5.3	20	31	114	C
72	Jan. 19, 1988	0730:31.9	-24.71	-70.57	6.3	6.7	0.41E+15	0.35E+20	3.5	356	11	90	F
73	Feb. 5, 1988	1401:02.8	-24.75	-70.43	6.2	6.7	0.29E+15	0.66E+20	1.3	287	31	40	M
74	Feb. 5, 1988	1849:31.8	-24.89	-70.55	6.0	6.1	0.20E+14	0.41E+19	1.5	62	29	125	M
75	March 9, 1988	2133:53.8	-17.33	-74.15	6.0	5.9	0.13E+14	0.91E+18	4.3	122	36	249	C
76	Aug. 14, 1988	1753:09.8	-27.26	-71.09	5.7	6.5	0.98E+14	0.11E+20	2.7	9	10	79	F
77	April 20, 1989	0808:51.1	-9.26	-79.03	5.8	.	0.12E+14	0.31E+18	11.6	335	40	276	C
78	June 25, 1989	2037:32.5	1.13	-79.62	5.9	6.1	0.30E+14	0.34E+19	2.6	13	17	90	F
79	Jan. 7, 1990	0906:43.4	-15.95	-74.25	5.9	5.3	0.14E+14	0.19E+18	22.1	161	52	140	C
80	April 21, 1990	1854:52.5	-36.99	-73.30	6.0	5.7	0.89E+13	0.66E+18	4.0	352	17	80	C
81	May 30, 1990	0234:05.9	-6.02	-77.23	6.1	6.5	0.12E+15	0.77E+19	4.7	160	26	109	M
82	Sept. 2, 1990	0426:48.1	-0.14	-80.28	5.8	6.1	0.26E+14	0.26E+19	3.0	340	8	90	F
83	April 4, 1991	1523:20.7	-6.04	-77.13	6.0	6.3	0.36E+14	0.45E+19	2.4	5	73	45	F
84	April 5, 1991	0419:49.5	-5.98	-77.09	6.5	6.8	0.94E+15	0.30E+20	9.4	64	51	26	M
85	April 5, 1991	1550:47.3	-14.23	-75.51	5.7	5.8	0.15E+14	0.30E+19	1.5	13	21	338	C
86	Nov. 19, 1991	2228:51.1	4.55	-77.44	6.4	7.0	0.57E+15	0.73E+20	2.3	268	57	5	F
<i>Southern Antilles</i>													
87	Dec. 28, 1991	0052:10.2	-56.10	-24.61	6.1	6.7	0.96E+15	0.90E+19	32.0	139	46	306	M
<i>New Zealand</i>													
88	Sept. 3, 1987	0640:13.9	-58.89	158.51	5.9	7.3	0.86E+15	0.14E+21	1.8	155	69	188	C
89	May 23, 1989	1054:46.3	-52.34	160.57	6.4	8.2	0.97E+17	0.14E+22	20.8	34	69	170	C
90	May 31, 1989	0554:20.6	-45.38	167.09	5.8	6.3	0.11E+15	0.53E+19	6.2	41	33	161	C
91	May 13, 1990	0423:09.6	-40.30	176.06	6.0	6.3	0.13E+14	0.46E+19	0.8	220	48	143	M
92	Sept. 17, 1990	1347:26.6	-53.15	159.63	6.0	6.0	0.20E+16	0.45E+19	133.3	115	87	10	F
<i>Tonga-Kermadec Region</i>													
93	Oct. 6, 1987	0419:06.1	-17.94	-172.23	6.7	7.3	0.49E+16	0.89E+20	16.5	307	64	209	M
94	Nov. 1, 1987	0842:06.5	-28.67	-177.55	6.1	.	0.60E+14	0.23E+19	7.8	205	34	98	M
95	Jan. 12, 1988	0729:28.0	-28.83	-177.42	6.1	6.4	0.39E+14	0.79E+19	1.5	185	30	90	F
96	June 11, 1988	1217:27.0	-14.99	-173.47	5.9	6.1	0.69E+14	0.16E+19	12.9	33	56	7	M
97	Oct. 8, 1988	0446:24.5	-18.77	-172.41	6.6	6.8	0.59E+15	0.48E+20	3.7	210	55	90	F
98	Oct. 10, 1988	1820:25.0	-28.64	-177.55	6.5	6.0	0.95E+13	0.31E+19	1.2	171	38	61	M
99	Dec. 5, 1988	1605:32.8	-15.26	-173.52	6.0	6.3	0.16E+15	0.31E+19	15.5	304	81	40	F
100	Dec. 16, 1988	0957:16.6	-29.79	-177.91	6.1	6.2	0.71E+14	0.49E+19	4.3	196	35	100	M
101	Feb. 25, 1989	1126:35.5	-29.92	-177.88	6.1	6.7	0.12E+15	0.14E+20	2.6	137	38	27	M
102	May 14, 1989	0059:50.5	-30.52	-178.41	5.9	6.6	0.39E+14	0.25E+20	0.5	185	30	90	F
103	May 20, 1989	1601:43.6	-30.51	-178.27	5.7	5.9	0.46E+13	0.28E+19	0.5	202	31	101	C
104	Aug. 14, 1989	1751:08.8	-19.02	176.65	5.8	5.9	0.20E+16	0.29E+19	206.9	148	82	180	F
105	Jan. 4, 1990	0532:21.0	-15.40	-172.85	6.4	6.4	0.10E+15	0.67E+19	4.5	140	60	270	F
106	Jan. 18, 1990	1245:23.6	-30.14	-177.69	6.0	5.8	0.29E+13	0.12E+19	0.7	134	27	51	M
107	March 3, 1990	1216:28.0	-22.12	175.16	6.3	7.4	0.17E+16	0.30E+21	1.7	135	83	156	F
108	April 6, 1990	1431:46.1	-21.62	-174.21	5.5	6.4	0.24E+13	0.17E+18	4.2	213	24	101	C
109	April 9, 1990	0931:09.6	-25.81	-176.06	5.7	5.9	0.33E+13	0.90E+18	1.1	353	31	258	C
110	Sept. 8, 1990	2031:57.8	-20.55	-174.17	5.6	5.7	0.34E+13	0.12E+19	0.8	160	14	90	F
111	Oct. 2, 1990	1506:44.6	-24.04	-174.65	5.8	5.5	0.92E+14	0.51E+18	54.1	38	84	5	F
112	Dec. 11, 1990	1441:42.5	-15.46	-173.12	5.8	6.1	0.94E+13	0.25E+19	1.1	305	54	152	M
113	Dec. 21, 1990	0529:28.7	-20.47	-174.16	6.1	6.2	0.95E+15	0.18E+19	158.3	30	90	8	F
114	Jan. 8, 1991	2204:09.5	-18.06	-173.53	6.1	6.0	0.17E+14	0.20E+19	2.5	163	57	90	F
115	March 3, 1991	1520:24.7	-21.87	-175.06	6.0	6.1	0.81E+13	0.20E+19	1.2	194	36	59	F
116	April 6, 1991	1434:20.7	-15.01	-175.52	5.8	6.7	0.42E+16	0.11E+20	114.5	112	85	358	M
117	Sept. 21, 1991	1519:48.2	-16.23	-173.00	5.8	5.7	0.42E+13	0.15E+19	0.8	115	43	31	M
118	Oct. 17, 1991	0905:20.2	-15.30	-173.56	5.6	6.1	0.67E+13	0.13E+19	1.5	135	11	124	M
119	Nov. 1, 1991	1623:22.4	-30.25	-177.98	6.4	6.5	0.44E+14	0.94E+19	1.4	202	30	99	C

Table 5. (continued)

No.	Origin		Latitude, deg	Longitude, deg	m_b	M_S	E_S , N m	M_0 , N m	τ_a	θ , deg	δ , deg	λ , deg	Reference
	Date	Time											
<i>Vanuatu</i>													
120	Jan. 3, 1987	2204:04.8	-15.00	167.93	6.0	6.5	0.13E+15	0.12E+20	3.2	4	38	90	F
121	Feb. 11, 1987	0756:12.9	-15.83	167.35	5.9	6.4	0.11E+15	0.48E+19	6.9	315	40	62	C
122	April 21, 1987	1528:39.8	-22.74	170.26	6.0	6.0	0.37E+14	0.17E+19	6.5	116	42	305	M
123	July 6, 1987	0249:42.8	-14.07	167.83	5.9	6.6	0.84E+14	0.96E+19	2.6	159	42	84	C
124	Aug. 14, 1987	0559:04.2	-12.58	166.59	5.6	5.8	0.42E+14	0.10E+19	12.6	18	39	88	M
125	Sept. 28, 1987	1147:08.6	-18.41	168.06	5.7	6.8	0.67E+14	0.19E+20	1.1	15	24	115	M
126	Sept. 28, 1987	1346:13.9	-18.55	168.16	5.8	6.5	0.83E+14	0.76E+19	3.3	352	23	95	M
127	May 3, 1988	2322:07.7	-22.77	170.28	5.9	5.8	0.61E+15	0.14E+19	130.7	308	86	230	F
128	May 16, 1988	2307:36.6	-13.94	166.34	6.0	5.7	0.15E+14	0.12E+19	3.7	355	45	270	F
129	June 12, 1988	1339:37.5	-10.75	165.17	5.7	6.4	0.10E+15	0.69E+19	4.3	342	24	90	F
130	June 27, 1988	0607:50.9	-20.24	169.37	5.8	.	0.64E+13	0.13E+19	1.5	126	18	4	C
131	July 23, 1988	1425:36.8	-22.13	174.90	5.9	6.4	0.44E+14	0.44E+19	3.0	232	35	5	M
132	July 31, 1988	1250:07.8	-22.21	171.08	5.8	6.3	0.48E+14	0.82E+19	1.8	98	68	5	M
133	Sept. 25, 1989	1417:47.1	-20.35	169.28	6.1	6.3	0.50E+14	0.58E+19	2.6	336	40	90	F
134	Feb. 19, 1990	0648:10.1	-15.47	166.38	6.4	6.7	0.19E+15	0.17E+20	3.4	246	35	353	C
135	March 5, 1990	1638:12.6	-18.32	168.06	5.6	7.0	0.13E+15	0.33E+20	1.2	350	28	104	C
136	Aug. 10, 1990	0537:52.2	-20.20	168.33	5.8	5.6	0.13E+14	0.57E+18	6.8	188	57	270	F
137	Dec. 22, 1990	1901:41.8	-14.95	168.04	5.8	5.4	0.99E+13	0.44E+18	6.7	16	69	35	F
138	Aug. 14, 1991	1915:03.7	-13.59	167.61	6.1	6.6	0.28E+15	0.66E+19	12.7	101	62	18	C
139	Oct. 12, 1991	1626:24.9	-13.74	166.67	5.9	6.1	0.25E+14	0.23E+19	3.3	334	37	74	M
<i>Solomon Islands Region</i>													
140	Feb. 7, 1984	2133:21.4	-10.01	160.47	6.6	7.5	0.75E+16	0.21E+21	10.7	295	39	30	E
141	Aug. 21, 1987	1822:37.5	-5.48	151.73	5.7	5.7	0.11E+13	0.91E+18	0.4	256	31	87	M
142	Oct. 16, 1987	2048:01.6	-6.27	149.06	5.9	7.4	0.23E+15	0.13E+21	0.5	266	32	90	C
143	Jan. 13, 1988	1623:13.6	-4.65	153.15	5.8	5.5	0.11E+14	0.86E+18	3.8	20	70	148	F
144	March 20, 1988	1041:51.1	-9.99	153.82	5.8	5.2	0.28E+14	0.48E+18	17.5	215	43	287	C
145	April 25, 1988	1010:33.8	-7.79	158.26	6.1	6.0	0.13E+15	0.24E+19	16.2	92	51	310	M
146	July 5, 1988	2032:07.2	-5.96	148.78	6.0	6.8	0.41E+14	0.15E+20	0.8	281	44	81	M
147	July 23, 1988	1517:08.2	-6.53	152.78	6.7	6.7	0.48E+15	0.32E+20	4.5	104	40	268	M
148	Aug. 6, 1988	0626:55.6	-7.14	151.06	5.9	5.7	0.47E+14	0.12E+19	11.7	50	22	90	F
149	Aug. 10, 1988	0438:26.2	-10.37	160.82	6.1	7.4	0.35E+15	0.25E+21	0.4	350	14	90	F
150	Nov. 18, 1988	1938:54.6	-6.13	149.79	5.8	6.4	0.28E+14	0.82E+19	1.0	218	47	67	M
151	Jan. 17, 1989	0035:23.2	-6.15	148.95	5.9	6.4	0.43E+14	0.50E+19	2.6	315	20	90	F
152	Feb. 4, 1989	2210:38.9	-4.63	153.07	6.1	.	0.33E+14	0.24E+19	4.1	311	43	139	M
153	Feb. 14, 1989	0620:21.3	-10.45	161.37	6.0	6.4	0.96E+14	0.58E+19	5.0	359	87	270	F
154	May 15, 1989	2334:33.7	-9.80	159.53	5.9	5.9	0.12E+15	0.84E+18	42.9	95	85	16	F
155	Oct. 17, 1989	1627:52.9	-4.03	152.41	5.6	5.8	0.17E+14	0.14E+19	3.6	140	70	17	C
156	Oct. 18, 1989	1140:50.2	-10.15	161.06	6.1	5.7	0.28E+14	0.11E+19	7.6	320	45	90	F
157	Oct. 27, 1989	2104:51.8	-11.02	162.35	6.1	7.0	0.12E+15	0.29E+20	1.2	345	9	90	F
158	July 10, 1990	0317:59.3	-10.35	161.12	6.0	.	0.67E+13	0.44E+19	0.5	100	85	315	F
159	Aug. 17, 1990	1307:17.4	-11.16	162.00	5.9	6.8	0.23E+14	0.13E+20	0.5	358	12	90	F
160	Nov. 22, 1990	2049:06.7	-5.57	150.99	6.0	6.0	0.14E+14	0.28E+19	1.5	244	41	74	M
161	Jan. 9, 1991	1508:53.6	-5.40	151.84	5.9	5.9	0.14E+13	0.21E+19	0.2	278	27	90	F
162	Feb. 9, 1991	1618:58.4	-9.93	159.14	6.4	6.9	0.24E+15	0.28E+20	2.6	270	25	270	F
163	Feb. 14, 1991	1922:15.2	-6.28	154.70	5.8	5.6	0.70E+12	0.92E+18	0.2	280	37	90	F
164	Sept. 28, 1991	2026:56.2	-5.81	150.96	5.8	6.6	0.13E+14	0.82E+19	0.5	259	33	63	M
165	Oct. 14, 1991	1558:12.8	-9.09	158.44	6.3	7.1	0.40E+15	0.78E+20	1.5	300	29	51	C
166	Nov. 4, 1991	0624:02.6	-6.07	148.20	5.7	6.0	0.22E+13	0.22E+19	0.3	253	38	72	M
<i>New Guinea Region</i>													
167	Feb. 8, 1987	1833:58.4	-6.09	147.69	0.0	7.4	0.23E+16	0.11E+21	6.3	351	88	180	M
168	June 27, 1987	0017:04.6	-2.16	138.17	5.7	6.5	0.14E+15	0.82E+19	5.1	15	86	159	F
169	Oct. 25, 1987	1654:05.7	-2.32	138.36	6.2	7.0	0.52E+15	0.19E+20	8.2	25	58	148	F
170	April 8, 1988	2313:24.1	-3.41	145.70	5.6	6.4	0.24E+15	0.49E+19	14.7	8	85	180	F
171	July 25, 1988	0646:06.7	-6.08	133.67	6.5	6.7	0.66E+16	0.28E+20	70.7	262	49	306	M
172	Aug. 1, 1989	0018:04.9	-4.51	139.02	6.0	5.8	0.48E+14	0.17E+19	8.5	322	13	90	F
173	Sept. 4, 1989	0520:55.9	-4.22	136.67	5.8	6.0	0.25E+14	0.38E+19	2.0	291	25	81	M
174	Nov. 3, 1989	1739:10.9	-1.28	148.71	5.7	5.7	0.92E+14	0.10E+19	27.6	127	87	145	F
175	Nov. 25, 1989	0749:44.2	-2.18	138.86	5.9	5.7	0.23E+14	0.13E+19	5.3	156	26	121	M
176	June 7, 1990	0925:19.2	-3.56	144.43	5.9	6.5	0.32E+15	0.58E+19	16.6	83	89	0	F
177	June 23, 1990	0501:44.5	-0.61	146.47	5.9	6.0	0.11E+14	0.22E+19	1.5	161	62	201	C
178	Jan. 3, 1991	1318:49.3	-7.18	148.54	6.0	6.0	0.92E+14	0.15E+19	18.4	260	75	335	F
179	Jan. 25, 1991	1738:36.5	-2.15	139.02	5.9	5.9	0.22E+14	0.19E+19	3.5	143	18	90	F
180	April 23, 1991	0248:58.5	-2.76	134.43	5.8	5.6	0.45E+14	0.00E+00	0.0	285	80	344	F
181	May 17, 1991	0231:25.7	-4.39	142.71	5.8	.	0.55E+14	0.38E+19	4.3	330	72	178	M
182	Dec. 29, 1991	1839:09.4	-4.42	132.73	6.0	6.1	0.35E+15	0.42E+19	25.0	317	80	190	F
<i>Caroline Islands</i>													
183	July 3, 1988	1143:12.7	8.92	137.90	5.9	6.3	0.13E+15	0.60E+19	6.5	33	35	80	C

Table 5. (continued)

No.	Origin		Latitude, deg	Longitude, deg	m_b	M_S	E_S , N m	M_0 , N m	τ_a	θ , deg	δ , deg	λ , deg	Reference
	Date	Time											
<i>Marianas Region</i>													
184	Dec. 15, 1987	1457:40.2	23.43	142.91	5.8	5.7	0.52E+13	0.98E+18	1.6	121	29	64	M
185	April 5, 1990	2112:35.5	15.13	147.60	6.5	7.5	0.44E+16	0.16E+21	8.2	84	38	316	M
186	April 6, 1990	1457:20.1	15.18	147.60	5.9	6.1	0.11E+15	0.23E+19	14.3	159	70	193	M
187	Sept. 23, 1990	2113:07.4	33.27	138.64	6.0	6.5	0.17E+16	0.71E+19	71.8	152	84	184	F
188	Sept. 3, 1991	0844:48.6	33.65	138.78	5.9	6.4	0.89E+15	0.28E+19	95.4	305	85	185	F
189	Nov. 11, 1991	2234:40.9	24.70	142.57	6.0	5.8	0.21E+14	0.53E+18	11.9	267	44	241	M
<i>Japan-Kurils-Kamchatka</i>													
190	June 29, 1980	0720:05.5	34.81	139.18	5.8	6.2	0.48E+15	0.41E+19	35.1	258	78	165	E
191	May 26, 1983	0259:59.6	40.46	139.10	6.8	7.7	0.72E+16	0.63E+21	3.4	360	30	90	E
192	June 21, 1983	0625:27.3	41.35	139.10	6.7	6.9	0.52E+15	0.21E+20	7.4	15	25	90	E
193	Nov. 22, 1986	0041:42.9	34.44	139.52	5.8	5.8	0.12E+15	0.90E+18	40.0	188	77	5	F
194	Nov. 30, 1986	2015:30.3	38.85	141.95	6.0	6.0	0.73E+13	0.11E+19	2.0	164	23	51	F
195	Jan. 9, 1987	0614:44.9	39.90	141.68	6.4	.	0.14E+15	0.88E+19	4.8	57	13	136	C
196	Feb. 6, 1987	1223:48.0	36.99	141.79	5.9	6.1	0.38E+14	0.44E+19	2.6	192	13	68	F
197	Feb. 6, 1987	1316:17.9	36.99	141.69	6.1	6.3	0.32E+15	0.13E+20	7.4	30	70	70	F
198	April 7, 1987	0040:43.4	37.36	141.80	6.4	6.6	0.20E+15	0.11E+20	5.5	237	19	129	M
199	April 22, 1987	2013:23.2	37.15	141.57	6.1	6.6	0.65E+14	0.11E+20	1.8	213	18	90	F
200	June 13, 1987	1400:39.3	44.67	150.39	5.8	5.8	0.17E+14	0.26E+18	19.6	220	18	90	F
201	Sept. 4, 1987	0427:08.9	49.29	156.41	5.9	6.2	0.25E+14	0.28E+19	2.7	215	22	90	F
202	Oct. 4, 1987	1027:20.3	37.31	141.62	5.8	5.0	0.13E+14	0.36E+18	10.8	171	47	64	F
203	Oct. 4, 1987	1834:22.6	55.58	161.62	6.0	5.4	0.29E+14	0.91E+18	9.6	163	39	40	M
204	Oct. 6, 1987	2011:35.1	52.96	159.97	6.1	6.3	0.23E+14	0.62E+19	1.1	225	29	102	M
205	Dec. 17, 1987	0208:19.9	35.36	140.21	6.0	.	0.19E+16	0.71E+19	80.3	67	75	0	F
206	July 6, 1988	1554:19.1	41.74	144.20	5.9	6.3	0.23E+14	0.25E+19	2.8	197	24	101	M
207	July 30, 1988	2107:21.2	44.77	149.89	6.3	.	0.56E+14	0.50E+18	33.6	183	39	28	C
208	Sept. 26, 1988	0823:19.8	35.53	141.07	5.9	5.5	0.24E+14	0.44E+18	16.4	220	49	90	F
209	Jan. 9, 1989	1342:36.4	46.99	153.48	6.0	6.4	0.93E+14	0.56E+19	5.0	217	8	90	F
210	Jan. 22, 1989	2220:18.0	41.81	144.28	6.0	6.3	0.41E+14	0.20E+19	6.1	269	19	152	M
211	March 6, 1989	1439:42.7	35.54	140.44	5.9	5.6	0.25E+14	0.15E+19	5.0	201	21	112	C
212	April 11, 1989	0356:36.9	49.49	159.18	6.3	6.6	0.30E+15	0.15E+20	6.0	230	68	270	F
213	Oct. 26, 1989	1706:41.6	39.81	143.54	5.8	5.8	0.14E+14	0.11E+19	3.8	205	8	90	F
214	Oct. 27, 1989	0145:55.1	39.82	143.69	5.8	6.2	0.21E+14	0.22E+19	2.9	195	5	90	F
215	Oct. 29, 1989	0525:38.3	39.57	143.33	6.0	6.6	0.85E+14	0.58E+19	4.4	210	5	90	F
216	Nov. 1, 1989	1825:34.9	39.84	142.76	6.4	7.4	0.12E+16	0.14E+21	2.6	271	39	158	M
217	Dec. 21, 1989	1649:13.2	45.36	150.11	5.9	5.8	0.96E+13	0.13E+19	2.2	190	25	90	F
218	Feb. 20, 1990	0653:39.9	34.71	139.25	6.1	6.4	0.53E+15	0.43E+19	37.0	70	82	173	F
219	March 31, 1990	1931:42.8	42.89	146.97	5.9	5.8	0.87E+13	0.13E+19	2.0	295	31	161	M
220	June 1, 1990	0122:11.6	35.52	140.34	5.7	.	0.11E+14	0.27E+19	1.2	134	18	78	M
221	Aug. 5, 1990	0336:22.3	36.31	141.07	5.8	6.0	0.45E+13	0.15E+19	0.9	228	26	99	M
222	Dec. 19, 1990	1348:22.7	52.62	160.72	5.9	5.6	0.64E+13	0.90E+18	2.1	207	35	79	C
223	Feb. 16, 1991	0123:40.4	48.27	154.33	6.3	5.7	0.14E+14	0.15E+19	2.8	230	12	90	F
224	May 7, 1991	1309:28.8	39.43	144.71	6.4	5.8	0.27E+15	0.11E+19	73.6	171	64	200	F
225	Aug. 6, 1991	1449:30.6	35.72	141.04	5.9	5.7	0.15E+14	0.76E+18	5.9	52	77	45	F
226	Aug. 26, 1991	1459:44.9	42.10	144.63	5.8	5.7	0.70E+13	0.40E+18	5.2	79	33	270	C
227	Nov. 26, 1991	1940:48.6	42.05	142.52	6.1	.	0.39E+14	0.46E+19	2.5	259	23	144	M
228	Nov. 27, 1991	0503:31.4	48.24	154.81	5.9	5.5	0.40E+13	0.50E+18	2.4	223	30	90	F
229	Dec. 13, 1991	0233:51.8	45.58	151.56	6.1	6.6	0.35E+14	0.81E+19	1.3	230	25	105	C
230	Dec. 13, 1991	0545:29.0	45.57	151.53	6.0	5.7	0.16E+13	0.10E+19	0.5	244	21	119	C
231	Dec. 13, 1991	1859:06.6	45.52	151.71	6.1	6.4	0.32E+14	0.54E+19	1.8	235	25	90	F
232	Dec. 13, 1991	1955:09.6	45.44	151.27	5.9	6.3	0.17E+14	0.39E+19	1.3	212	23	75	M
233	Dec. 15, 1991	1016:58.6	45.12	151.37	5.7	5.3	0.51E+12	0.19E+18	0.8	285	33	153	M
234	Dec. 19, 1991	0133:40.4	45.25	151.18	6.0	6.6	0.46E+14	0.15E+20	0.9	55	66	60	F
235	Dec. 22, 1991	0843:13.4	45.53	151.02	6.3	7.4	0.51E+15	0.28E+21	0.5	235	20	90	F
236	Dec. 23, 1991	1310:04.9	45.85	151.96	6.0	5.3	0.25E+14	0.17E+18	44.1	65	88	132	F
<i>Korea, China Sea, Ryukyu</i>													
237	March 18, 1987	0336:30.3	32.03	131.84	6.4	.	0.11E+15	0.12E+20	2.7	348	27	257	C
238	Jan. 3, 1989	0441:12.1	29.49	131.43	5.8	5.6	0.11E+14	0.56E+18	5.9	175	77	270	F
239	Feb. 17, 1990	0228:01.8	29.53	130.73	5.9	.	0.20E+14	0.18E+19	3.3	217	70	70	F
240	May 17, 1990	2328:00.1	26.62	127.85	6.0	5.7	0.60E+13	0.63E+18	2.9	231	28	101	C
<i>Taiwan</i>													
241	Nov. 14, 1986	2120:10.6	23.90	121.57	6.3	7.8	0.16E+16	0.13E+21	3.7	227	32	98	F
242	July 20, 1988	2315:36.7	23.90	121.60	5.8	5.7	0.99E+13	0.81E+18	3.7	237	33	121	C
243	Aug. 3, 1989	1131:20.4	23.04	121.96	5.9	6.4	0.14E+16	0.48E+19	87.5	130	87	5	F
244	Sept. 11, 1990	1409:02.5	22.69	120.91	5.8	5.6	0.99E+13	0.54E+18	5.5	345	27	57	C
245	Sept. 30, 1990	1905:02.5	24.25	125.21	5.9	6.2	0.89E+13	0.18E+19	1.5	280	11	153	F
246	Dec. 13, 1990	0301:48.0	23.92	121.64	5.9	6.2	0.26E+14	0.32E+19	2.4	235	16	90	F
247	Dec. 13, 1990	1950:17.9	23.72	121.63	5.9	6.3	0.33E+15	0.36E+19	27.5	11	85	166	F

Table 5. (continued)

No.	Origin		Latitude, deg	Longitude, deg	m_b	M_S	E_S , N m	M_0 , N m	τ_a	θ , deg	δ , deg	λ , deg	Reference
	Date	Time											
<i>Philippines Region</i>													
248	Dec. 29, 1986	1549:59.2	15.22	119.88	6.0	.	0.66E+13	0.65E+18	3.0	343	37	101	M
249	May 12, 1987	0130:25.0	7.09	126.70	6.2	6.4	0.90E+14	0.56E+19	4.8	150	23	90	F
250	June 6, 1987	1840:27.5	10.67	126.11	5.7	6.3	0.53E+14	0.57E+19	2.8	163	7	72	M
251	June 7, 1987	0549:43.6	20.43	121.37	5.8	6.1	0.46E+14	0.27E+19	5.1	355	35	57	C
252	June 14, 1987	0507:26.9	10.43	126.15	5.6	5.9	0.50E+13	0.25E+19	0.6	219	25	90	F
253	Nov. 18, 1987	1627:05.3	12.85	124.77	5.9	6.3	0.28E+14	0.41E+19	2.0	183	22	90	F
254	Feb. 24, 1988	0352:03.3	13.48	124.62	6.0	7.0	0.11E+16	0.86E+20	3.8	195	12	112	M
255	Nov. 17, 1988	0655:46.1	12.40	124.54	6.0	6.6	0.11E+15	0.90E+19	3.7	128	51	352	C
256	Aug. 12, 1989	1646:43.3	8.68	125.72	5.9	.	0.18E+14	0.74E+18	7.3	242	47	240	C
257	Dec. 15, 1989	1843:45.0	8.34	126.73	6.2	7.3	0.58E+15	0.24E+21	0.7	195	17	90	F
258	Dec. 20, 1989	0008:20.6	8.09	126.83	6.0	6.3	0.96E+14	0.68E+19	4.2	204	21	124	M
259	Feb. 8, 1990	0715:32.2	9.76	124.69	6.2	6.6	0.18E+15	0.15E+20	3.6	280	38	120	M
260	July 16, 1990	0726:34.6	15.68	121.17	6.5	7.8	0.19E+17	0.41E+21	13.9	167	69	18	F
261	July 17, 1990	2114:43.9	16.50	120.98	6.1	6.6	0.26E+15	0.62E+19	12.6	167	69	11	F
262	July 18, 1990	0800:12.9	16.51	121.01	5.8	5.3	0.12E+13	0.25E+18	1.4	214	39	85	C
263	Oct. 25, 1990	1101:38.7	8.31	126.46	5.9	6.1	0.21E+14	0.36E+19	1.7	163	42	55	C
264	Feb. 18, 1991	0237:25.1	8.87	126.48	6.0	6.6	0.50E+14	0.16E+20	0.9	139	26	57	F
265	Nov. 13, 1991	1112:13.2	8.36	126.37	6.1	6.4	0.12E+15	0.10E+20	3.6	175	25	90	F
<i>Borneo-Sulawesi</i>													
266	Jan. 29, 1987	0243:47.7	1.26	126.23	5.8	5.9	0.63E+14	0.46E+19	4.1	318	49	47	M
267	Nov. 27, 1987	0002:08.1	-0.23	125.06	5.8	5.7	0.79E+13	0.15E+19	1.6	232	33	121	C
268	Nov. 7, 1988	2315:41.8	1.53	126.36	6.2	.	0.15E+15	0.90E+18	50.0	97	37	288	C
269	Jan. 10, 1989	0555:01.5	-3.16	130.56	5.9	6.5	0.16E+15	0.12E+20	4.0	129	14	90	C
270	Feb. 10, 1989	1115:24.7	2.31	126.76	6.2	6.8	0.19E+16	0.54E+20	10.6	67	38	107	M
271	Feb. 27, 1989	2339:10.8	2.30	128.01	5.8	6.0	0.80E+14	0.39E+19	6.2	9	85	315	F
272	March 8, 1989	0234:25.9	-0.21	124.89	5.8	5.2	0.91E+13	0.73E+18	3.7	179	11	94	M
273	March 8, 1989	1144:32.3	1.03	126.19	5.9	5.6	0.39E+14	0.14E+19	8.4	265	50	127	M
274	Sept. 6, 1989	1445:51.0	0.98	126.11	5.8	5.5	0.92E+13	0.11E+19	2.5	154	43	49	C
275	April 18, 1990	1339:19.0	1.19	122.86	6.2	7.4	0.14E+16	0.33E+21	1.3	358	55	27	M
276	April 18, 1990	1832:60.0	1.32	123.02	5.9	6.2	0.13E+14	0.65E+19	0.6	98	24	99	C
277	April 19, 1990	1240:38.7	1.11	123.43	5.8	6.2	0.87E+14	0.34E+19	7.7	350	84	315	F
278	April 26, 1990	1540:34.4	1.06	122.82	5.8	5.8	0.13E+14	0.90E+18	4.3	18	22	54	M
279	May 25, 1990	0203:27.6	-2.87	130.34	5.8	5.4	0.24E+14	0.72E+18	10.0	109	8	74	M
280	Aug. 10, 1990	1544:31.4	0.33	126.18	5.8	.	0.16E+14	0.25E+19	1.9	231	50	128	C
281	Aug. 25, 1990	1547:53.9	0.52	126.08	6.0	6.1	0.62E+14	0.40E+19	4.6	35	38	90	F
282	Dec. 13, 1990	1226:40.8	1.12	124.03	6.0	5.7	0.15E+15	0.15E+19	30.0	165	49	127	M
283	May 19, 1991	0058:01.7	1.16	122.96	6.0	6.8	0.12E+15	0.25E+20	1.4	250	85	142	F
284	June 20, 1991	0518:52.5	1.20	122.79	6.2	7.0	0.30E+15	0.23E+21	0.4	96	15	88	M
285	Aug. 8, 1991	0209:44.7	0.97	122.63	5.9	6.4	0.22E+14	0.90E+19	0.7	75	12	90	F
<i>Sunda Arc</i>													
286	Dec. 19, 1986	0341:55.3	-9.92	119.20	5.7	6.2	0.10E+15	0.43E+19	7.0	25	63	171	M
287	June 17, 1987	0132:53.7	-5.58	130.79	6.6	.	0.22E+16	0.48E+20	13.7	305	50	142	C
288	Nov. 26, 1987	0143:14.1	-8.25	124.15	5.8	6.5	0.65E+15	0.80E+19	24.4	3	89	359	M
289	Dec. 17, 1987	2022:58.4	-9.17	114.61	5.7	5.5	0.79E+13	0.12E+19	2.0	238	72	310	F
290	Aug. 17, 1988	0159:07.7	-7.70	107.15	6.1	5.8	0.14E+14	0.12E+19	3.5	102	43	96	M
291	July 14, 1989	2042:40.1	-8.08	125.13	6.4	6.2	0.57E+15	0.11E+20	15.5	240	54	70	F
292	July 31, 1989	1707:27.9	-8.05	121.38	6.3	6.2	0.43E+15	0.11E+20	11.7	83	45	139	C
293	July 6, 1990	0016:20.4	-6.90	108.12	5.8	4.8	0.24E+13	0.23E+18	3.1	303	40	90	F
294	Oct. 15, 1990	0135:44.6	-2.21	92.25	5.9	6.5	0.13E+16	0.14E+20	27.9	105	90	190	F
295	March 5, 1991	2235:48.1	-3.98	102.37	5.9	.	0.24E+14	0.44E+18	16.4	118	60	125	F
296	May 21, 1991	1100:19.1	-7.52	126.54	6.2	6.3	0.19E+15	0.87E+19	6.6	95	22	90	F
297	July 2, 1991	0514:30.2	-1.07	99.84	5.8	6.1	0.85E+13	0.35E+19	0.7	135	55	39	F
298	July 4, 1991	1143:10.5	-8.10	124.68	6.2	6.5	0.38E+15	0.15E+20	7.6	250	67	27	F
299	July 5, 1991	0430:52.5	-9.59	114.67	5.7	5.6	0.45E+13	0.16E+19	0.8	340	8	163	C
300	Dec. 22, 1991	2115:42.4	-4.89	103.18	5.8	.	0.26E+12	0.14E+18	0.6	272	29	64	C
<i>Southeast Asia</i>													
301	Nov. 6, 1988	1303:19.3	22.79	99.61	6.1	7.3	0.31E+16	0.37E+20	25.1	333	78	174	C
302	Jan. 5, 1991	1457:11.6	23.61	95.90	6.2	7.1	0.19E+16	0.31E+20	18.4	275	88	355	F
<i>India-Tibet-South China</i>													
303	Aug. 20, 1988	2309:09.6	26.75	86.62	6.4	6.6	0.23E+15	0.23E+20	3.0	120	82	125	F
304	April 15, 1989	2034:08.9	29.99	99.19	6.2	6.2	0.10E+15	0.53E+19	5.7	85	40	270	F
305	April 25, 1989	0213:20.8	30.05	99.42	6.2	6.0	0.51E+14	0.18E+19	8.5	75	45	270	F
306	May 3, 1989	0553:01.2	30.09	99.47	6.1	6.1	0.48E+14	0.22E+19	6.5	240	44	243	C
307	May 3, 1989	1541:30.9	30.05	99.50	5.8	5.9	0.39E+14	0.56E+18	20.9	111	68	329	F
308	June 12, 1989	0004:09.8	21.86	89.76	6.1	5.1	0.50E+14	0.58E+18	25.9	354	67	164	C
309	Sept. 22, 1989	0225:50.9	31.58	102.43	6.1	6.1	0.83E+14	0.18E+19	13.8	227	70	152	F
310	Oct. 19, 1991	2123:14.3	30.78	78.77	6.5	7.0	0.32E+15	0.18E+20	5.3	18	38	172	M

Table 5. (continued)

No.	Origin		Latitude, deg	Longitude, deg	m_b	M_s	E_s , N m	M_0 , N m	τ_a	θ , deg	δ , deg	λ , deg	Reference
	Date	Time											
<i>Central Northern China</i>													
311	Dec. 22, 1987	0016:39.0	41.36	89.64	5.9	5.2	0.66E+14	0.21E+18	94.3	186	49	128	C
312	Nov. 5, 1988	0214:30.3	34.35	91.88	5.9	6.3	0.82E+13	0.26E+19	0.9	136	43	80	M
313	Jan. 14, 1990	0303:19.2	37.82	91.97	6.1	6.1	0.24E+14	0.11E+19	6.5	94	41	116	M
314	April 17, 1990	0159:33.4	39.44	74.90	6.0	6.2	0.42E+14	0.12E+19	10.5	126	66	166	M
315	April 26, 1990	0937:15.0	35.99	100.25	6.5	6.9	0.21E+15	0.56E+19	11.2	123	35	61	M
<i>Central Asia</i>													
316	June 14, 1990	1247:28.8	47.87	85.08	6.1	6.8	0.36E+15	0.90E+19	12.0	292	83	157	F
317	Aug. 3, 1990	0915:06.2	47.96	84.96	6.0	6.1	0.58E+14	0.20E+19	8.7	225	82	45	F
318	Nov. 12, 1990	1228:51.5	42.96	78.07	5.9	6.3	0.61E+14	0.33E+19	5.5	211	65	23	C
319	Dec. 27, 1991	0909:37.5	51.02	98.15	5.8	6.4	0.11E+15	0.38E+19	8.7	75	90	1	F
<i>Western Asia, Iran, Afghan</i>													
320	March 19, 1984	2028:38.2	40.32	63.35	6.5	7.0	0.43E+15	0.28E+20	4.6	230	35	90	J
321	Dec. 18, 1987	1624:03.0	28.19	56.68	5.8	5.5	0.29E+14	0.67E+18	13.0	186	36	254	M
322	Sept. 16, 1989	0205:08.9	40.34	51.53	6.4	6.5	0.16E+15	0.45E+19	10.7	305	78	270	F
323	Sept. 17, 1989	0053:39.8	40.20	51.75	6.1	6.1	0.65E+14	0.22E+19	8.9	292	36	245	C
324	June 20, 1990	2100:10.0	36.96	49.41	6.4	7.7	0.11E+17	0.14E+21	23.6	288	88	349	F
325	June 21, 1990	0902:14.6	36.64	49.80	5.8	5.3	0.98E+13	0.49E+18	6.0	204	26	121	C
326	Nov. 6, 1990	1845:52.2	28.25	55.46	6.2	6.7	0.48E+14	0.83E+19	1.7	245	35	90	F
<i>Middle East, Crimea, Balkans</i>													
327	Dec. 7, 1988	0741:24.2	40.99	44.19	6.2	6.8	0.39E+15	0.17E+20	6.9	310	60	125	I
328	April 29, 1991	0912:48.1	42.45	43.67	6.2	7.0	0.14E+15	0.33E+20	1.3	288	39	106	C
329	April 29, 1991	1830:41.5	42.50	43.90	5.9	6.0	0.74E+13	0.16E+19	1.4	87	43	90	M
330	June 15, 1991	0059:20.3	42.46	44.01	6.1	6.1	0.20E+14	0.29E+19	2.1	325	30	90	F
331	July 18, 1991	1156:30.6	44.89	22.41	5.7	5.5	0.11E+13	0.29E+18	1.1	313	47	294	M
<i>Mediterranean Area</i>													
332	Oct. 10, 1980	1225:23.5	36.19	1.35	6.5	7.3	0.21E+15	0.23E+20	2.7	240	60	90	J
333	Oct. 29, 1989	1909:12.9	36.79	2.45	5.7	5.7	0.45E+13	0.90E+18	1.5	91	48	119	C
334	Dec. 21, 1990	0657:43.0	41.00	22.30	5.8	5.9	0.75E+13	0.17E+19	1.3	249	41	288	C
<i>Atlantic Ocean</i>													
335	April 20, 1988	0425:36.6	0.96	-30.27	5.8	5.3	0.41E+13	0.20E+18	6.1	319	22	35	C
336	May 20, 1988	1458:43.5	8.11	-38.41	5.8	5.9	0.29E+15	0.12E+19	72.5	102	90	180	F
337	June 11, 1989	1324:32.1	35.11	-35.01	5.8	5.5	0.10E+15	0.63E+18	47.6	330	82	178	M
338	June 26, 1989	1038:39.5	39.11	-28.24	5.7	5.7	0.60E+14	0.54E+18	33.3	188	75	8	M
339	July 14, 1990	0554:25.5	0.00	-17.38	6.2	6.4	0.74E+15	0.86E+19	25.8	160	90	8	F
340	Feb. 10, 1991	1242:37.6	8.74	-39.85	5.9	5.9	0.10E+15	0.88E+18	34.1	270	90	187	F
341	June 10, 1991	1735:49.5	23.77	-45.37	6.1	6.5	0.13E+15	0.33E+19	11.8	225	78	27	F
<i>Indian Ocean</i>													
342	Sept. 23, 1987	1514:56.3	-50.72	139.28	5.8	6.1	0.12E+15	0.22E+19	16.4	272	51	163	M
343	Feb. 26, 1988	0617:31.5	-37.32	47.99	6.1	6.7	0.29E+15	0.18E+20	4.8	328	26	122	M
344	Jan. 6, 1990	2144:56.3	-10.68	92.99	5.7	5.5	0.77E+13	0.12E+19	1.9	8	25	52	C
345	Feb. 22, 1990	1651:51.1	-11.46	66.38	5.7	5.6	0.16E+15	0.55E+18	87.3	220	83	358	M
346	Dec. 28, 1990	2232:17.3	-14.88	66.78	6.0	5.8	0.57E+15	0.88E+18	194.3	165	86	358	F
347	Jan. 13, 1991	1154:36.7	-2.93	84.57	5.9	5.3	0.33E+15	0.59E+18	167.8	0	0	0	F
348	May 13, 1991	1628:15.4	-3.46	82.82	5.9	5.4	0.56E+13	0.10E+19	1.7	134	46	129	M
<i>Eastern North America</i>													
349	Jan. 9, 1982	1253:51.7	46.98	-66.57	5.7	5.2	0.27E+13	0.25E+18	3.2	195	65	70	J
350	Jan. 11, 1982	2141:08.0	46.97	-66.67	5.4	4.5	0.30E+13	0.67E+17	13.4	340	45	75	J
351	Oct. 28, 1983	1406:06.6	44.06	-113.59	6.2	7.3	0.32E+15	0.17E+20	5.6	160	55	-65	A
352	Nov. 25, 1988	2346:04.5	48.12	-71.18	5.9	5.8	0.17E+14	0.88E+18	5.8	189	39	135	J
353	Dec. 25, 1989	1424:32.6	60.08	-73.44	6.2	6.3	0.41E+13	0.66E+18	1.9	45	55	90	J
<i>Africa</i>													
354	Dec. 13, 1982	0912:48.0	14.70	44.38	6.0	6.0	0.48E+14	0.30E+19	4.8	340	60	300	B
355	Oct. 25, 1987	1646:13.4	5.41	36.75	5.6	6.2	0.16E+14	0.25E+19	1.9	238	27	204	M
356	March 10, 1989	2149:45.9	-13.70	34.42	6.2	6.1	0.98E+14	0.31E+19	9.5	165	33	293	M
357	Aug. 20, 1989	1116:56.5	11.77	41.94	5.8	6.3	0.96E+13	0.62E+19	0.5	284	33	268	M
358	Aug. 20, 1989	1925:56.5	11.90	41.82	6.2	5.7	0.90E+13	0.16E+19	1.7	285	34	268	C
359	Aug. 21, 1989	0109:06.6	11.87	41.87	6.3	6.2	0.57E+14	0.53E+19	3.2	271	32	264	M
360	Aug. 21, 1989	0503:05.6	11.94	41.77	5.8	5.7	0.67E+13	0.16E+19	1.3	274	34	252	M
361	May 20, 1990	0222:01.6	5.12	32.15	6.7	7.1	0.14E+16	0.53E+20	7.9	250	80	176	F
362	May 24, 1990	1934:44.2	5.28	31.83	5.9	6.6	0.24E+14	0.64E+19	1.1	74	37	279	M
363	May 24, 1990	2000:08.2	5.36	31.85	6.5	7.0	0.33E+15	0.48E+20	2.1	232	43	229	C
364	July 9, 1990	1511:20.4	5.39	31.65	5.9	6.4	0.15E+14	0.33E+19	1.4	28	44	211	C
365	April 21, 1991	2312:22.5	-18.29	46.42	5.8	5.3	0.11E+14	0.24E+18	13.7	22	41	259	M

Table 5. (continued)

No.	Origin		Latitude, deg	Longitude, deg	m_b	M_S	E_S , N m	M_0 , N m	τ_a	θ , deg	δ , deg	λ , deg	Reference
	Date	Time											
<i>Australia</i>													
366	June 2, 1979	0947:58.7	-30.73	117.21	6.0	6.1	0.49E+13	0.14E+19	1.0	190	40	90	J
367	March 30, 1986	0853:53.2	-26.19	132.77	5.8	5.8	0.18E+13	0.50E+18	1.1	145	42	76	J
368	Jan. 22, 1988	0035:58.1	-19.91	133.81	6.1	6.3	0.50E+14	0.29E+19	5.2	100	35	90	G
369	Jan. 22, 1988	0357:25.2	-19.81	133.90	6.1	6.4	0.15E+15	0.52E+19	8.7	290	70	120	G
370	Jan. 22, 1988	1204:57.5	-19.88	133.88	6.5	6.3	0.40E+15	0.83E+19	14.5	100	45	80	G
371	Jan. 22, 1988	2054:03.0	-19.86	133.99	5.8	5.0	0.50E+13	0.10E+18	15.0	110	50	50	G
<i>Pacific Basin</i>													
372	March 7, 1988	1521:06.8	41.67	152.22	5.9	5.1	0.14E+14	0.22E+18	19.1	199	40	113	C
373	June 26, 1989	0327:04.0	19.36	-155.08	5.8	6.1	0.40E+14	0.52E+19	2.3	238	7	99	C
<i>Arctic Region</i>													
374	May 25, 1987	1131:54.3	63.85	-19.73	5.8	5.8	0.15E+15	0.11E+19	40.9	194	85	178	M
375	March 21, 1988	2331:21.7	77.60	125.45	6.0	6.0	0.96E+14	0.43E+19	6.7	185	16	296	M
<i>Eastern Asia, Sakhalin, Okhotsk</i>													
376	April 20, 1989	2259:54.1	57.17	121.98	6.1	6.5	0.47E+14	0.31E+19	4.5	7	19	145	M
377	Nov. 13, 1990	0235:07.9	46.10	138.64	6.2	5.7	0.79E+13	0.83E+18	2.9	196	45	83	C
<i>NE Asia, Northern Alaska, Greenland</i>													
378	Oct. 5, 1985	1524:02.2	62.24	-124.27	6.5	6.6	0.18E+15	0.12E+20	4.5	170	30	107	J
379	Dec. 23, 1985	0516:03.3	62.22	-124.24	6.4	6.9	0.28E+15	0.18E+20	4.7	177	22	116	J
380	March 25, 1988	1936:46.5	62.15	-124.18	6.1	6.0	0.46E+14	0.24E+19	5.8	170	30	90	J
381	March 8, 1991	1136:28.4	60.90	167.02	6.4	6.6	0.10E+15	0.10E+20	3.0	47	17	90	F
<i>SE Pacific</i>													
382	July 6, 1987	0106:07.7	-27.00	-108.29	6.2	6.3	0.26E+15	0.14E+20	5.6	29	18	241	M
383	Aug. 21, 1990	1413:04.8	-27.49	-104.27	6.0	5.3	0.14E+14	0.11E+19	3.8	49	30	269	M
384	Sept. 3, 1991	0905:28.3	-17.91	-116.00	6.0	5.9	0.13E+15	0.37E+19	10.5	233	47	316	M
385	Sept. 3, 1991	1156:16.3	-17.92	-115.99	5.8	5.9	0.28E+14	0.32E+19	2.6	169	30	288	M
386	Dec. 11, 1991	1703:10.6	-17.82	-116.02	5.9	6.1	0.16E+14	0.48E+19	1.0	34	50	226	M
<i>Andaman to Sumatera</i>													
387	April 3, 1988	1427:09.1	4.69	94.42	5.9	5.7	0.48E+14	0.73E+18	19.7	93	40	65	M
388	Jan. 22, 1990	1726:11.4	3.88	96.10	6.0	5.8	0.15E+14	0.25E+19	1.8	313	27	89	C
389	Nov. 15, 1990	0234:32.4	3.91	97.46	6.0	6.8	0.11E+15	0.12E+20	2.7	125	67	174	M
390	Nov. 15, 1990	0448:12.2	3.98	97.32	5.8	5.6	0.12E+14	0.00E+00	0.0	215	60	90	F
391	Nov. 18, 1990	1623:06.9	3.94	97.34	5.7	.	0.24E+12	0.20E+18	0.4	300	48	110	F
392	July 23, 1991	1325:47.3	3.78	95.93	5.8	5.1	0.16E+13	0.33E+18	1.5	218	27	37	M
393	Aug. 6, 1991	0217:31.6	3.83	95.37	6.0	5.3	0.74E+13	0.37E+18	6.0	158	17	84	M
<i>Afghan-Kashmir</i>													
394	March 4, 1990	1946:19.7	28.92	66.33	5.8	6.1	0.62E+13	0.14E+19	1.3	235	55	45	F
395	June 17, 1990	0451:45.5	27.40	65.72	5.9	6.3	0.33E+14	0.18E+19	5.5	207	45	15	M
396	July 26, 1990	0653:56.4	27.25	65.51	5.8	5.8	0.34E+14	0.76E+18	13.4	225	83	20	F
<i>Hindu-Kush, Pamir</i>													
397	Oct. 26, 1984	2022:21.8	39.15	71.24	6.0	6.1	0.30E+14	0.21E+19	4.3	42	64	34	J

Radiated energy and seismic moment of 397 shallow earthquakes are given as a function of seismic region. The origin times, locations, and magnitudes are taken from the Monthly Listings of the Preliminary Determination of Epicenters (PDE). The energies (E_S), moments (M_0), and focal mechanisms are from the PDE except where a special study is indicated. Read $0.11E+20$ as 0.11×10^{20} . The last column gives the reference for the focal mechanism (given by strike (θ), dip (δ), and slip (λ)) that is regarded as the most consistent with energy radiation. Where taken from the PDE, the focal mechanism type is indicated by F (first-motion), M (body wave moment tensor), or C (centroid moment tensor). Any other letter indicates that E_S , M_0 , and focal mechanism were taken from a special study: A, Boatwright and Choy [1986]; B, Choy and Kind [1987]; D, Choy and Dewey [1988]; E, Boatwright and Choy [1989]; G, Choy and Bowman [1990]; H, Choy and Boatwright [1990]; I, Choy and Kind [1990]; J, Boatwright and Choy [1992]. Apparent stress (τ_a) is in bars.

Acknowledgments. This research was partially supported by the Nuclear Regulatory Commission under contract RES82001. The authors are grateful to James W. Dewey, Steve Mueller, William Spence, Heidi Houston, Gregory Beroza, and Masayuki Kikuchi for reviews and valuable comments. The authors are also grateful for the assistance of Christina K. LaVonne, Russell E. Needham, and Madeleine Zirbes in the processing and analysis of global network data.

References

Barrientos, S. E., Slip distribution of the 1985 central Chile earthquake, *Tectonophysics*, **145**, 225–241, 1988.

Bergman, E. A., Intraplate earthquakes and the state of stress in oceanic lithosphere, *Tectonophysics*, **132**, 1–35, 1986.

Bergman, E. A., and S. C. Solomon, On the strength of oceanic fracture zones and their influence on the intraplate stress field, *J. Geophys. Res.*, **97**, 15,365–15,377, 1992.

Beroza, G. C., and T. H. Jordan, Searching for slow and silent earthquakes using free oscillations, *J. Geophys. Res.*, **95**, 2485–2510, 1990.

Boatwright, J., and G. L. Choy, Teleseismic estimates of the energy radiated by shallow earthquakes, *J. Geophys. Res.*, **91**, 2095–2112, 1986.

Boatwright, J., and G. L. Choy, Acceleration spectra for subduction zone earthquakes, *J. Geophys. Res.*, **94**, 15,541–15,553, 1989.

- Braunmiller, J., and J. Nábělek, Rupture process of the Macquarie Ridge earthquake of May 23, 1989, *Geophys. Res. Lett.*, *17*, 1017–1020, 1990.
- Chamot-Rooke, N., and X. LePichon, Zenisu Ridge: Mechanical model of formation, *Tectonophysics*, *160*, 175–193, 1989.
- Choy, G. L., and J. Boatwright, The rupture characteristics of two deep earthquakes inferred from broadband GDSN data, *Bull. Seismol. Soc. Am.*, *71*, 691–711, 1981.
- Choy, G. L., and J. Boatwright, Teleseismic and near-field analysis of the Nahanni earthquakes in the Northwest Territories, Canada, *Bull. Seismol. Soc. Am.*, *78*, 1627–1652, 1988.
- Choy, G. L., and J. Boatwright, Source characteristics of the Loma Prieta, California, earthquake of October 18, 1989, from global digital seismic data, *Geophys. Res. Lett.*, *17*, 1183–1186, 1990.
- Choy, G. L., and J. R. Bowman, Rupture process of a multiple main shock sequence: Analysis of teleseismic, local and field observations of the Tennant Creek, Australia, earthquakes of January 22, 1988, *J. Geophys. Res.*, *95*, 7326–7342, 1990.
- Choy, G. L., and V. F. Cormier, Direct measurement of the mantle attenuation operator from broadband *P* and *S* waveforms, *J. Geophys. Res.*, *91*, 7326–7342, 1986.
- Choy, G. L., and J. W. Dewey, Rupture process of an extended earthquake sequence: Teleseismic analysis of the Chilean earthquake of March 3, 1985, *J. Geophys. Res.*, *93*, 1103–1118, 1988.
- Choy, G. L., and R. Kind, Rupture complexity of a moderate-sized (m_b 6.0) earthquake: Broadband body-wave analysis of the north Yemen earthquake of 13 December 1982, *Bull. Seismol. Soc. Am.*, *77*, 28–46, 1987.
- Choy, G. L., and R. Kind, A preliminary broadband body-wave analysis of the Armenia S. S. R. earthquake of 7 December 1988: *Geol. Jahrb.*, *44*, 37–48, 1990.
- Christensen, D. H., and L. J. Ruff, Rupture process of the March 3, 1985 Chilean earthquake, *Geophys. Res. Lett.*, *13*, 721–724, 1986.
- Cormier, V. F., The effect of attenuation on seismic body waves, *Bull. Seismol. Soc. Am.*, *72*, s169–s200, 1982.
- Dziewonski, A. M., T. A. Chou, and J. H. Woodhouse, Determination of earthquake source parameters from waveform data for studies of global regional seismicity, *J. Geophys. Res.*, *86*, 2825–2852, 1981.
- Ekström, G., and B. Romanowicz, The 23 May 1989 Macquarie Ridge earthquake: A very broad band analysis, *Geophys. Res. Lett.*, *17*, 993–996, 1990.
- Flinn, E. A., E. R. Engdahl, and A. R. Hill, Seismic and geographical regionalization, *Bull. Seismol. Soc. Am.*, *64*, 771–992, 1974.
- Hanks, T., and W. Thatcher, A graphical representation of seismic source parameters, *J. Geophys. Res.*, *77*, 4393–4405, 1972.
- Harvey, D., and G. L. Choy, Broadband deconvolution of GDSN data, *Geophys. J. R. Astron. Soc.*, *69*, 659–668, 1982.
- Houston, H., Broadband source spectra, seismic energies, and stress drops of the 1989 Macquarie Ridge earthquake, *Geophys. Res. Lett.*, *17*, 1021–1024, 1990.
- Kanamori, H., The energy release in great earthquakes, *J. Geophys. Res.*, *82*, 2981–2987, 1977.
- Kanamori, H., and C. R. Allen, Earthquake repeat time and average stress drop, *Earthquake Source Mechanics, Geophys. Monogr. Ser.*, vol. 37, edited by S. Das, J. Boatwright, and C. H. Scholz, pp. 227–235, AGU, Washington, D. C., 1986.
- Kikuchi, M., and Y. Fukao, Seismic wave energy inferred from long-period body wave inversion, *Bull. Seismol. Soc. Am.*, *78*, 1707–1724, 1988.
- Lahr, J., R. A. Page, and C. D. Stevens, Unusual earthquakes in the Gulf of Alaska and fragmentation of the Pacific Plate, *Geophys. Res. Lett.*, *15*, 1483–1486, 1988.
- Monfret, T., and B. Romanowicz, Importance of on scale observations of first arriving Rayleigh wave trains for source studies: Example of the Chilean event of March 3, 1985, observed in the Geoscope and IDA networks, *Geophys. Res. Lett.*, *13*, 1015–1018, 1986.
- Mueller, S., and R. J. Phillips, On the initiation of subduction, *J. Geophys. Res.*, *96*, 651–665, 1991.
- Park, J., Radial mode observations from the 5/23/89 Macquarie Ridge earthquake, *Geophys. Res. Lett.*, *17*, 1005–1008, 1990.
- Richards, M. A., and D. C. Engebretson, Transform faults—A guiding force of plate tectonics, *Eos Trans. AGU*, *75*(16), Spring Meet. Suppl., 63, 1994.
- Ruff, L. J., J. W. Given, C. O. Sanders, and C. M. Sperber, Large earthquakes in the Macquarie Ridge Complex: Transitional tectonics and subduction initiation, *Pure Appl. Geophys.*, *129*, 71–129, 1989.
- Satake, K., and H. Kanamori, Fault parameters and tsunami excitation of the May 23, 1989, Macquarie Ridge earthquake, *Geophys. Res. Lett.*, *17*, 997–1000, 1990.
- Severinghaus, J. P., and K. C. Macdonald, High inside corners at ridge-transform intersections, *Mar. Geophys. Res.*, *9*, 353–367, 1989.
- Silver, P. G., and T. H. Jordan, Total-moment spectra of fourteen large earthquakes, *J. Geophys. Res.*, *88*, 3273–3293, 1983.
- Sipkin, S. A., Estimation of earthquake source parameters by the inversion of waveform data: synthetic seismograms, *Phys. Earth Planet. Inter.*, *30*, 242–259, 1982.
- Sipkin, S. A., Estimation of earthquake source parameters by the inversion of waveform data: Global seismicity, 1981–1983, *Bull. Seismol. Soc. Am.*, *76*, 1515–1541, 1986.
- Snoke, J. A., A. T. Linde, and I. S. Sacks, Apparent stress: An estimate of the stress drop, *Bull. Seismol. Soc. Am.*, *73*, 339–348, 1983.
- Tichelaar, B. W., and L. J. Ruff, Rupture process and stress drop of the great 1989 Macquarie Ridge earthquake, *Geophys. Res. Lett.*, *17*, 1001–1004, 1990.
- Wyss, M., and J. N. Brune, Seismic moment, stress, and source dimensions for earthquakes in the California-Nevada regions, *J. Geophys. Res.*, *73*, 4681–4694, 1968.

J. L. Boatwright, U.S. Geological Survey, 345 Middlefield Road, MS 977, Menlo Park, CA 94025.

G. L. Choy, U.S. Geological Survey, National Earthquake Information Center, Denver Federal Center, Box 25046, MS 967, Denver, CO 80225. (e-mail: choy@neis.cr.usgs.gov)

(Received July 12, 1994; revised June 15, 1995; accepted June 20, 1995.)